

# Carbon Nanomaterials for Next-Generation Interconnects and Passives: Physics, Status, and Prospects

Hong Li, *Student Member, IEEE*, Chuan Xu, *Student Member, IEEE*, Navin Srivastava, *Student Member, IEEE*, and Kaustav Banerjee, *Senior Member, IEEE*

(Invited Paper)

**Abstract**—This paper reviews the current state of research in carbon-based nanomaterials, particularly the one-dimensional (1-D) forms, carbon nanotubes (CNTs) and graphene nanoribbons (GNRs), whose promising electrical, thermal, and mechanical properties make them attractive candidates for next-generation integrated circuit (IC) applications. After summarizing the basic physics of these materials, the state of the art of their interconnect-related fabrication and modeling efforts is reviewed. Both electrical and thermal modeling and performance analysis for various CNT- and GNR-based interconnects are presented and compared with conventional interconnect materials to provide guidelines for their prospective applications. It is shown that single-walled, double-walled, and multiwalled CNTs can provide better performance than that of Cu. However, in order to make GNR interconnects comparable with Cu or CNT interconnects, both intercalation doping and high edge-specularity must be achieved. Thermal analysis of CNTs shows significant advantages in tall vias, indicating their promising application as through-silicon vias in 3-D ICs. In addition to on-chip interconnects, various applications exploiting the low-dimensional properties of these nanomaterials are discussed. These include chip-to-packaging interconnects as well as passive devices for future generations of IC technology. Specifically, the small form factor of CNTs and reduced skin effect in CNT interconnects have significant implications for the design of on-chip capacitors and inductors, respectively.

**Index Terms**—Capacitor, carbon nanomaterials, double-walled carbon nanotube (CNT), energy storage, graphene nanoribbon (GNR), high-frequency, inductor, interconnects, multiwalled CNT, single-walled CNT, skin effect, through-silicon vias (TSVs).

Manuscript received February 18, 2009. Current version published August 21, 2009. This work was supported by the National Institute of Standards and Technology under Grant 70NANB5H1215, and the National Science Foundation under Grant CCF-0811880 and Grant CCF-0917385. The review of this paper was arranged by Editor S. Saha.

H. Li, C. Xu, and K. Banerjee are with the Department of Electrical and Computer Engineering, University of California, Santa Barbara, CA 93106 USA (e-mail: hongli@ece.ucsb.edu; chuanxu@ece.ucsb.edu; kaustav@ece.ucsb.edu).

N. Srivastava was with the Department of Electrical and Computer Engineering, University of California, Santa Barbara, CA 93106 USA. He is now with the Mentor Graphics Corporation, Wilsonville, OR 97070 USA (e-mail: navins@ece.ucsb.edu).

Color versions of one or more of the figures in this paper are available online at <http://ieeexplore.ieee.org>.

Digital Object Identifier 10.1109/TED.2009.2026524

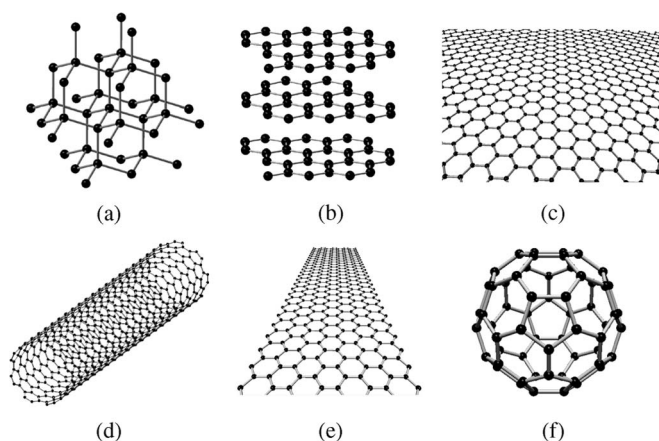


Fig. 1. Some allotropes of carbon exhibiting different dimensionalities. Except diamond (a), which is an  $sp^3$ -bonded structure, other allotropes (b)–(f) are  $sp^2$  bonded and can be regarded as derivatives of 2-D graphene (c). (a) Three-dimensional diamond. (b) Three-dimensional graphite. (c) Two-dimensional graphene. (d) One-dimensional nanotube. (e) One-dimensional nanoribbon. (f) Zero-dimensional fullerenes.

## I. INTRODUCTION

**A** CARBON ATOM with its distinct types of valence bonds forms various allotropes [1], as shown in Fig. 1. While its 3-D structures, namely, diamond and graphite, are well-known, it also forms low-dimensional allotropes collectively known as carbon nanomaterials, such as 1-D carbon nanotubes (CNTs) [2] and 0-D fullerenes [3]. Graphene, a 2-D single layer of graphite, is the most recent addition to this list since its discovery a few years ago [4], although its electronic structure and properties have been theoretically studied as far back as 1947 [5].

Carbon nanomaterials have extraordinary physical properties that make them exciting prospects for a variety of applications in microelectronics/nanoelectronics [6], [7], spintronics [8], [9], optics [10], as well as material science [11], mechanical [12] and biological fields [13], and even fundamental areas like relativistic quantum mechanics and condensed matter physics [14]. Particularly in the nanoelectronics area, CNTs and graphene nanoribbons (GNRs) have aroused a lot of interest in their applications as energy storage (such as supercapacitors [15]), energy conversion devices (including thermoelectric [16]

TABLE I  
PROPERTIES OF CARBON NANOMATERIALS RELEVANT TO VLSI  
INTERCONNECTS AND PASSIVES

	Cu	SWCNT	MWCNT	Graphene or GNR
Max current density (A/cm <sup>2</sup> )	10 <sup>7</sup>	>10 <sup>9</sup> [32]	>10 <sup>9</sup> [33]	>10 <sup>8</sup> [4]
Melting point (K)	1356	3800 (graphite)		
Tensile strength (GPa)	0.22	22.2±2.2 [34]	11-63 [12]	
Thermal conductivity (×10 <sup>3</sup> W/m-K)	0.385	1.75-5.8 [35]	3 [37]	3-5 [38],[39]
Temperature Coefficient of Resistance (×10 <sup>-3</sup> /K)	4	<1.1 [40]	-1.37 [41]	-1.47 [42]
Mean free path (nm) @ room temperature	40	>10 <sup>3</sup> [43]	2.5×10 <sup>4</sup> [44] *	1×10 <sup>3</sup> [45]

\* MFP of MWCNTs depends on their diameters. The measured value shown here is for the MWCNT with outmost shell diameter of 100 nm.

and photovoltaic [17] devices), field emission displays and radiation sources [18], nanometer semiconductor transistors [4], [19]–[22], nanoelectromechanical systems (NEMS) [23], [24], electrostatic discharge (ESD) protection [25], as well as interconnects [26]–[29] and passives [30], [31], due to their extraordinary electrical, thermal, and mechanical properties [4], [12], [32]–[46]. A summary of the key properties of carbon nanomaterials relevant to this paper is provided in Table I. The  $sp^2$  bonding in these materials, which is stronger than the  $sp^3$  bonds in diamond, makes graphene the strongest material ever measured [47]. The properties of graphite, which is also an  $sp^2$ -bonded structure, provide first hints toward the remarkable properties of CNTs and GNRs. The charge carrier densities in graphite are almost equal for electrons and holes ( $n_e \approx n_h \approx 7 \times 10^{18}/\text{cm}^3$ ) and measured mobilities are on the order of  $10^4 \text{ cm}^2/\text{V} \cdot \text{s}$  at room temperature and  $10^6 \text{ cm}^2/\text{V} \cdot \text{s}$  at 4.2 K [48]. Graphene and CNTs also have very high current carrying capability (at least two orders of magnitude higher than that of Cu) [4], [32], [33]. In addition, CNT and GNR are found to have long mean free paths (MFPs) at low bias due to weak acoustic phonon scattering and suppressed optical phonon scattering at room temperature [43], [49]. Unlike the scattering mechanisms in a 3-D conductor, where scattering can occur at small angles and the required momentum is relatively low, the backscattering (180° angle) in 1-D conductor requires much higher momentum and thus the scattering is weak, leading to larger momentum relaxation time or mean free path. All of these unique properties indicate that CNT and GNR could be potentially employed as alternative materials for next-generation nanoscale interconnects, which can enhance the electrical performance as well as eliminate electromigration reliability concerns that plague nanoscale Cu interconnects [50], [51].

As reliability concerns put a question mark on the continued use of Cu (due to increasing resistivity, current density, and on-chip metal temperatures) at the nanoscale [52]–[54], this paper provides a comprehensive review of the physics of these carbon nanomaterials, current status of their fabrication and modeling, and their prospects for replacing standard interconnect metals in applications ranging from on-chip interconnections to energy storage and packaging elements for integrated circuit (IC) applications. It provides an overview of the state of the art of CNT and GNR interconnect-related fabrication and modeling

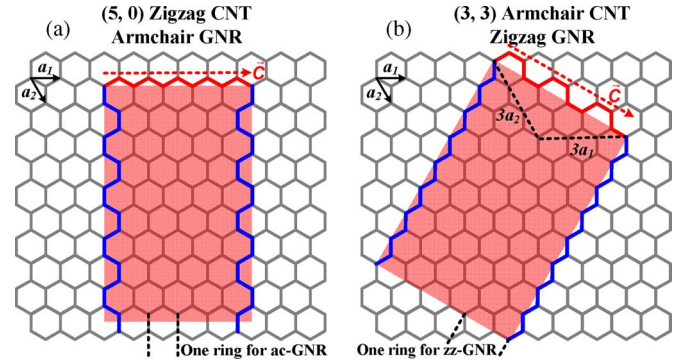


Fig. 2. Schematic view of CNT and GNR made from a graphene sheet. (a) zz-CNT and ac-GNR. (b) ac-CNT and zz-GNR. The unit lattice vectors of graphene  $a_1$  and  $a_2$  are shown at the upper-left corners. The dashed arrows represent the circumferential vector  $\vec{C}$  of CNT. Red lattice lines indicate the circumference shape of CNT, and blue lattice lines indicate two possible edge shapes of GNR.

efforts. In addition, it presents a comparative analysis of these materials with standard interconnect materials, thereby providing guidelines for their design and fabrication in prospective applications. It also proposes novel passive devices (inductors and capacitors) based on CNTs for energy storage applications by exploiting their specific low-dimensional properties.

This paper is organized as follows. Section II introduces the basic physics of carbon nanomaterials. Recent progress and remaining challenges in the fabrication of these materials are outlined in Section III. Detailed discussion of both electrical and thermal modeling of carbon nanomaterials is presented in Section IV. Various applications for these materials are explored in Section V, including on-chip interconnects and passive devices, through-silicon vias (TSVs) in 3-D ICs, and off-chip/packaging applications. Finally, Section VI draws a brief summary.

## II. PHYSICS OF CARBON NANOMATERIALS

Nanostructures, such as CNTs and GNRs, have unique properties that include low-dimensional conduction and low density of states at the Fermi level [55]. Some of their fundamental properties relevant to interconnect applications are discussed in the following paragraphs.

### A. Crystal Structure of Carbon Nanomaterials

To understand the physics of CNTs or GNRs, it is necessary to study their atomic structure. Both CNTs and GNRs can be understood as structures derived from a graphene sheet, which is a single layer of carbon atoms packed into a 2-D honeycomb lattice structure. A CNT can be thought of as a rolled-up graphene sheet in which the edges of the sheet are joined together to form a seamless tube, while a GNR can be obtained by patterning graphene to a strip, as shown in Fig. 2.

The dashed arrows in Fig. 2 show the circumferential vector  $\vec{C}$ , whose direction is also the direction of the roll-up for a CNT. The vector is defined as  $\vec{C} = n \cdot \hat{a}_1 + m \cdot \hat{a}_2$ , where  $\hat{a}_1$  and  $\hat{a}_2$  are the lattice vectors of graphene, and  $n$  and  $m$  are the chiral indexes. As such, the chiral indexes  $(n, m)$  uniquely define the “chirality,” or the direction of the roll-up, for a CNT [1].

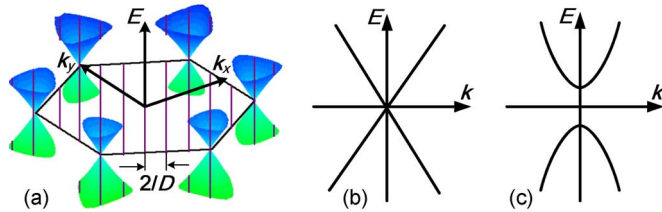


Fig. 3. (a) Band structure of graphene forms hexagonal cones in the vicinity of the Fermi energy. The apexes of the six cones are called Dirac points. The formation of a nanotube cuts the energy landscape into slices of allowed states (wave vector is quantized). The locations of the cross section of the cut lines in  $k$ -space with the cones determine whether the resulting band structure is (b) metallic or (c) semiconducting.

The length of  $\vec{C}$  is the circumference of CNT, from which its diameter  $D$  can be calculated as follows:

$$D = |\vec{C}|/\pi = \frac{a}{\pi} \sqrt{n^2 + m^2 + mn} \quad (1)$$

where  $a$  is the lattice constant of graphene ( $= 0.246$  nm). In Fig. 2(a), the circumferential vector  $\vec{C} = 5\hat{a}_1 + 0\hat{a}_2$ , hence, the CNT rolled up along  $\vec{C}$  is identified as  $(5, 0)$ . In this case, because the circumferential edge of CNT has a zigzag shape (shown in red), it is also called a zigzag CNT (zz-CNT). Similarly, for the case shown in Fig. 2(b), the CNT is identified with the chiral indexes  $(3, 3)$ , and because the circumferential edge of the CNT has armchair shape, it is called an armchair CNT (ac-CNT). All zz-CNTs have indexes  $n$  or  $m = 0$ , while ac-CNTs have  $n = m$ . The two cases shown in Fig. 2 are special cases where the circumferential vector of CNT is either along the lattice vectors ( $n$  or  $m = 0$ ) or along the exact direction between two vectors ( $n = m$ ). For other directions of circumferential vector, the CNTs are called “chiral.”

The chirality of a GNR, on the other hand, is defined by the edge shape as shown in Fig. 2 (in blue), which is perpendicular to the circumferential vector for a CNT. As a result, the GNR (shaded) in Fig. 2(a) is armchair, while the one in Fig. 2(b) is zigzag.

## B. Electrical Properties

The band structure of graphene is the basis for understanding the electronic behavior of CNTs and GNRs. The Brillouin zone of graphene is shown in Fig. 3(a), where the cones represent the electron energy dispersion of graphene close to the Fermi energy. It can be calculated by a simple tight-binding approach [1]. The band structure of graphene is unique in the sense that the  $E-k$  relation is linear for lowest energies near the six corners of the 2-D hexagonal Brillouin zone, leading to zero effective mass for electrons and holes [56] (for more details, see the Appendix I). Due to this linear “dispersion” relation at low energies, electrons and holes near these six points behave like relativistic particles described by the Dirac equation for spin  $1/2$  particles [6]. Hence, the electrons and holes are called Dirac fermions, and the six corners of the Brillouin zone [the apexes of the six cones shown in Fig. 3(a)] are called the Dirac points.

Since a CNT can be regarded as a seamless rolled-up graphene sheet, it has periodic boundary conditions around the circumference. This periodicity requires that the wave vector

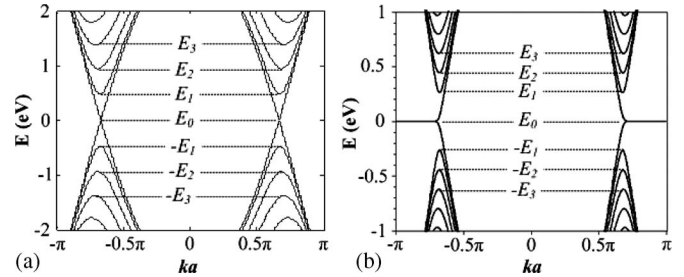


Fig. 4. Band structures of (a) ac-CNT ( $n = m = 20$ ,  $D = 2.7$  nm) and (b) zz-GNR ( $N = 26$ ,  $w = 11$  nm), where  $N$  is the number of hexagonal carbon rings across the width of GNR,  $w$  is the width of GNR, and  $a$  is the lattice constant.

along the circumference be quantized as  $|\vec{C}| = i\lambda$  or  $\vec{C} \cdot \vec{k} = 2\pi \cdot i$ , where  $i$  is a nonzero integer, and  $\lambda$  is the electron wave length. The quantization condition is reflected in the Brillouin zone as slices cut out of the band structure, indicated by the solid lines in Fig. 3(a). The separation between the slices is  $2\pi/|\vec{C}| = 2/D$ , and their orientation depends on the nanotube “chirality” or index  $(n, m)$  [55]. For a specific tube diameter and chirality, if there is a slice cut exactly at the apex of the cones [as in Fig. 3(a)], there is no bandgap between the conduction and valence bands, as shown in Fig. 3(b). Such nanotubes are metallic. If the slices cut elsewhere on the cones, there will be a bandgap around the Fermi energy, as shown in Fig. 3(c), and such nanotubes are semiconducting. The condition for achieving metallic tubes is expressed as  $n - m = 3i$ , where  $i$  is an integer [1] (for more details, see Appendix II). Hence, ac-CNTs are always metallic [see the bandstructure shown in Fig. 4(a)], while zz-CNTs could be metallic or semiconducting, depending on the chiral indexes  $(n, m)$ . For a natural mix of CNTs, statistically, one-third of the CNTs are metallic, and the other two-thirds are semiconducting [1]. Since the spacing of slices is inversely proportional to  $D$ , larger-diameter nanotubes have more slices with smaller spacing between slices, which leads to smaller bandgaps for semiconducting CNTs.

Although GNRs are also derivatives of graphene, the difference between CNTs and GNRs arises from the boundary condition: the wave function along the CNT circumference is periodic, while the wave function along the GNR width vanishes at the two edges. Thus, the wave vector quantization in GNR is  $w = i \cdot \lambda/2$  or  $w \cdot \vec{k} = \pi \cdot i$ , where  $w$  is the width of GNR, and  $i$  is an integer. Armchair GNRs (ac-GNRs) can be either metallic or semiconducting, depending on the number ( $N$ ) of hexagonal carbon rings (shown in Fig. 2) across the width: metallic when  $N = 3i - 1$  (the transverse wave vector with respect to the Dirac point,  $\Delta k_{\text{transverse}} = n\pi/w$ , where  $n$  is an integer; for  $n = 0$ ,  $\Delta k_{\text{transverse}} = 0$ , implying that the zeroth subbands pass through the Dirac points), and semiconducting when  $N = 3i$  or  $3i + 1$  ( $\Delta k_{\text{transverse}} = (n + 1/3)\pi/w$  or  $\Delta k_{\text{transverse}} = (n - 1/3)\pi/w$ , where  $i$  is an integer. In comparison, zigzag GNRs (zz-GNRs) are always metallic and independent of  $N$ . While the band structure of ac-GNRs are similar to that of zz-CNTs, the electronic states of zz-GNRs are more complicated than those of ac-CNTs. Particularly, the zz-GNRs have the “dispersionless band” or “zero mode,” which originates from the edge states [57], [58]:

TABLE II  
CONDITIONS OF METALLICITY FOR CNT AND GNR ( $n, m$  IS THE CHIRALITY INDEX OF CNT,  $N$  IS THE NUMBER OF HEXAGONAL CARBON RINGS, AND  $i$  IS AN INTEGER)

	Armchair	Zigzag	Chiral
CNT	metallic	$n$ or $m = 3i$	$n-m=3i$
GNR	$N=3i-1$	metallic ( $w > 10$ nm)	-

almost flatband appears within the region of  $2\pi/3 < |ka| \leq \pi$  [shown in Fig. 4(b)]. According to the band structure, zz-GNRs are always metallic. However, when wire width is smaller than 10 nm, neutral zz-GNRs will have small bandgap because of the staggered sublattice potential from magnetic ordering once electron spin is considered [19], [59]. The bandgap of zz-GNRs increases with decreasing wire width (the bandgap, in electronvolts, is  $0.933/(w + 1.5)$ , with  $w$  in nanometers).

Since the focus in this paper is on the metallicity of CNTs or GNRs, Table II summarizes the conditions of metallicity for both CNTs and GNRs.

### C. Heat Transport Properties

The measured high thermal conductivity of CNTs [35]–[37] and GNRs [38], [39] is higher than that of diamond ( $\sim 2000$  W/m · K). It is important to understand the heat transport mechanism in CNTs/GNRs to get an insight into their outstanding thermal properties. Since the following analysis will be valid for both CNTs and GNRs, we will only discuss the case of CNTs.

One important heat transport property of CNT (due to its low dimensionality) is the quantization of thermal conductance, which is theoretically analyzed in [60]. The quantum of thermal conductance  $G_0^{\text{th}}$ , is  $G_0^{\text{th}} = \pi^2 k_B^2 T / 3h$ , where  $k_B$  is Boltzmann's constant,  $T$  is the temperature, and  $h$  is Planck's constant. Recently, quantization of thermal conductance of CNT has been observed experimentally for individual CNTs [61] and agrees well with the theoretical prediction [62].

Another important heat transport property is that phonons dominate the heat conduction in CNTs, unlike electrons in traditional metals. According to the simultaneous measurement of thermal conductivity  $\kappa$  and electrical conductivity  $\sigma$  of SWCNT with a diameter of 1.4 nm, the measured value of  $\kappa/\sigma T$  is two orders of magnitude larger than the Lorentz number  $2.45 \times 10^{-8}$  W ·  $\Omega/\text{K}^2$  [35]. This implies that the electron contribution to heat transport is very small, and that Wiedemann–Franz law [63] will not be valid for CNTs. It is the phonon contribution that dominates the thermal conductance in CNTs. This can be understood from the different bandgaps of electron energy dispersion and phonon energy dispersion (Fig. 5). At low temperatures, thermal conductance of CNT is quantized, and the phonon contribution of thermal conductance  $G_{\text{ph}}^{\text{th}} = 4G_0^{\text{th}}$  due to four acoustic phonon modes [60]. Note that in Fig. 5, there are only three distinct acoustic phonon branches because there is degeneracy in transverse acoustic modes (the lowest acoustic phonon modes). The thermal conductance due to electrons satisfies Wiedemann–Franz law and can be calculated as  $G_{\text{el}}^{\text{th}} = 4G_0^{\text{th}}$  (theoretical electrical conductance  $G = 4e^2/h$  at low temperature), which is equal to the phonon thermal

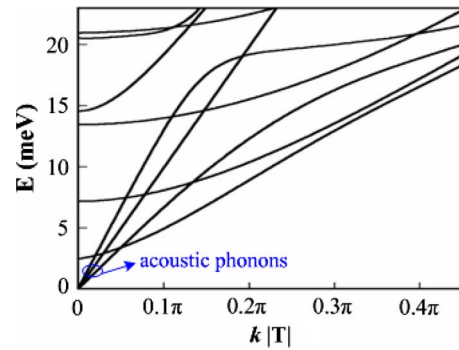


Fig. 5. Phonon dispersion of a (10, 10) armchair CNT. The three lines passing through the origin represent acoustic phonon modes, while others are optical phonon modes.  $\vec{T}$  is the translation vector, and its magnitude can be calculated by  $|\vec{T}| = 3^{1/2}\pi D/d_R$ , where  $d_R$  is the greatest common divisor of  $(2n + m, 2m + n)$  for  $(n, m)$  CNT [1].

conductance counterpart ( $G_{\text{ph}}^{\text{th}}$ ). However, when temperature increases, the number of contributing electron modes remains four due to the large energy gap between the lowest subbands (on the order of 100 meV, see Fig. 4), which implies that  $G_{\text{el}}^{\text{th}}$  remains at  $4G_0^{\text{th}}$ . However, as temperature increases, the population of phonon modes increases dramatically (governed by Bose–Einstein distribution) since the energy gap between the low energy phonon branches is typically less than 10 meV (see Fig. 5) [1]. As a result, the electron contribution to the heat transport becomes vanishingly small with increasing temperature. This has been theoretically shown in [60], where the  $G_{\text{el}}^{\text{th}}/G_{\text{ph}}^{\text{th}}$  decreases from 1 at low temperatures to  $< 0.1$  at room temperature. Since we are interested in IC applications, where the operating temperature is well above the room temperature, the dominant contribution to heat transport in CNTs will be from phonons.

## III. FABRICATION AND INTEGRATION

While CNT/GNR fabrication technologies have progressed rapidly since their inception, they are still relatively immature for integration into current very-large-scale integration (VLSI) technology. Since fabrication of interconnect will be a common basis of further applications (passive devices and off-chip) discussed in this paper, we will review the current status and challenges of CNT/GNR interconnect-related fabrication in this section.

### A. CNT Interconnect Fabrication

The high resistance (see Section IV-A) associated with an isolated CNT (greater than 6.45 k $\Omega$  for an SWCNT) necessitates the use of a bundle (rope) of CNTs [64], [65], conducting current in parallel to form a good electrical interconnection. For CNT interconnect applications, in order to outperform Cu, high density and high quality of CNT bundles will be preferred. The former requirement will increase the number of CNTs in a given area, which will increase the conductance accordingly, the latter one will reduce the defects and scatterings and result in long MFP and low resistance. As per a CMOS back-end process requirement, the growth temperature of CNT interconnects should be kept below 400 °C.

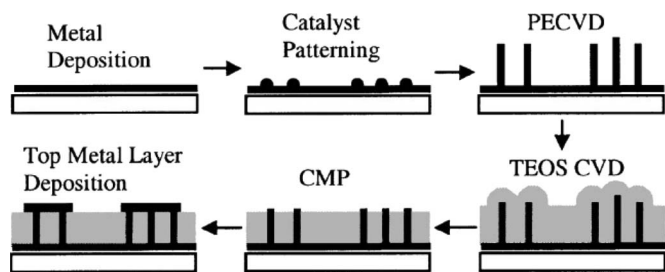


Fig. 6. Schematic of a “bottom-up” CNT process sequence [27].

Because of these requirements, chemical vapor deposition (CVD) methods are most suited for interconnect applications since they allow selective growth, large area deposition, and aligned CNT bundle growth. The growth temperature depends on the type of nanotube to be grown and the catalyst composition, and lies in the range from 400 °C to 1100 °C [66]. CVD methods first require preparation of metal catalyst particles on a substrate. The catalyst materials are transition metals (such as Fe, Co, and Ni). These catalyst particles are then submitted to a reduction treatment by heating with a reducing gas (such as H<sub>2</sub> or NH<sub>3</sub>). Finally, carbon-rich deposition gas (hydrocarbon gas, such as C<sub>2</sub>H<sub>2</sub>, and CH<sub>4</sub>) as a source is let into the furnace, where the hydrocarbon molecules are decomposed at the surface of the catalyst particles to allow carbon deposition at the edge of the particles, and therefore, CNTs are synthesized at the sites of the catalysts. Diameter of the nanotubes are determined by the size of the catalyst nano particles. The catalyst particles can stay at the tips of the growing nanotube during the growth process, or remain at the nanotube base on the substrate, depending on the adhesion between the catalyst particle and the substrate. Both SWCNT and MWCNT bundle can be grown using CVD methods on semiconductor wafers with standard semiconductor production equipment [67].

Until recently, it has been difficult to grow dense bundles of SWCNTs because the fertility of the catalyst particles for SWCNT growth was low. Although 84% catalyst activity has been reported in [68], the grown SWCNT bundle is very sparse, only occupying 3.6% of the total volume. Moreover, the lack of control on chirality means that it is difficult to ensure that the SWCNTs forming a bundle are all metallic. Although 87% metallic fraction (*F<sub>m</sub>*, fraction of metallic SWCNTs in a bundle) of SWCNT bundle has been reported [69], it is not suitable for large-scale integration and the density of bundle after separation is quite low. By using the zipping effect of liquids, [70] has demonstrated that the density of SWCNT bundle can be increased by 20 times, and more importantly, this highly densely packed SWCNT bundle retains the intrinsic properties of individual SWCNTs. More recently, homogeneous SWCNT films have been developed by assembling SWCNTs into a dense “CNT wafer,” enabling integration of nanodevice systems by lithography [71].

So far, most of the CNT interconnect fabrication work has focused on MWCNTs, since MWCNT is easier to be fabricated and always behaves as metallic. Two different approaches to integrate CNTs have been investigated. “Bottom-up” approach has been proposed in [27] as shown in Fig. 6, where the CNT via is grown on the bottom metal layer before deposition of

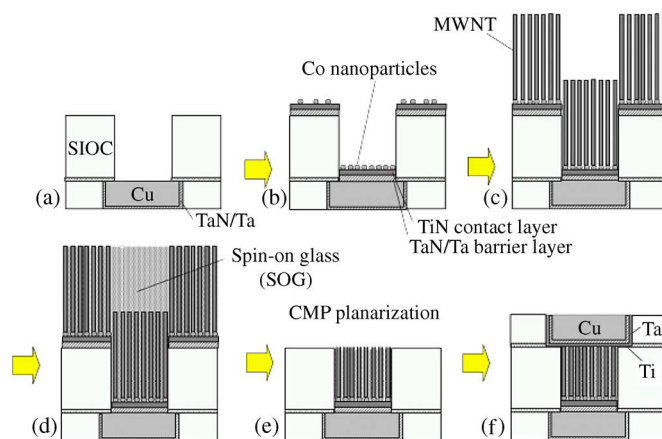


Fig. 7. CNT damascene via process proposed in [76]. (a) Via hole formation on bottom metal. (b) TaN/Ta barrier layer, TiN contact layer, and Co catalyst nanoparticle formation. (c) MWCNT growth all over the substrate. (d) SOG coating. (e) CMP planarization. (f) Top metal formation.

dielectric. One drawback of this approach is that the tubes do not always grow at the selected location and are sometimes shifted and tilted from the desired locations, which makes further processing quite challenging.

More conventionally, the etch-first approach has been pursued by several groups [26], [28], [72], where the dielectric is deposited and via holes are etched before growing nanotubes [shown in Fig. 7(a)]. In this approach, catalyst treatment is a critical issue to achieve good contact as well as good control of CNT size. The straightforward method is to deposit a thin catalyst layer into the etched via [26]. However, the contact condition between grown CNT and substrate might not be good in this method, and CNT growth can occur from the sidewalls of the via hole, which do not contribute to conductance. In order to grow CNTs in a controlled manner from the via bottom only and form contacts simultaneously, a buried catalyst approach has been developed in [73]. However, it is challenging to ensure etch stop on the thin catalyst layer with thickness of only 1–5-nm. A multilayer buried catalyst approach has also been developed to increase the CNT growth yield after via etching [74].

All the above methods, where the catalyst layer is either deposited or buried have a big issue that it is hard to control the number and size of catalyst particles when they are formed from the catalyst films, which, in turn, will affect the control of density and size of grown CNTs in the bundle. In order to solve this problem, a size-controlled catalyst nanoparticle deposition technique has been developed in [75], where a large number of particles are produced and selected through a size-controlled impactor before being injected into via holes. By using this technique, the diameter of the nanotube has been well controlled, and the density of CNTs achieved has been as high as  $9 \times 10^{11}/\text{cm}^2$  (diameter  $\sim 4$  nm, about 13% of volume fraction) [75], [76]. Fig. 7 shows the flow of CNT damascene via process developed in [76]. Moreover, the chemical–mechanical polishing (CMP) used in [76] not only planarizes the wafer, but also opens the nanotube ends for better contact with the second metal layer.

Most recently, low temperature (365 °C) growth has been achieved for on-chip CNT vias [29]. It has been shown that at low temperatures, CNT via can be successfully incorporated

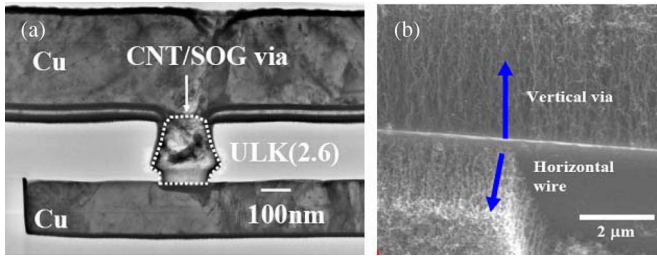


Fig. 8. (a) TEM image of the CNT via structure integrated with an ULK dielectric [29]. (b) SEM image of vertical and horizontal CNT bundles grown from a contact block [28].

in ultra-low- $k$  (ULK) dielectric ( $k = 2.6$ ) and showed no impact on electromigration reliability. Fig. 8(a) shows a Cu/ULK integrated CNT via structure. Growing well aligned high aspect ratio CNT bundle (length  $> 100 \mu\text{m}$ ) has also been demonstrated in [77] and [78], which could possibly be used as through-wafer vias in 3-D ICs. In addition, progress has also been recently reported on the densification of MWCNT bundles [79], which can increase CNT density by  $5 \sim 25$  times.

As discussed above, the current state of the art of on-chip integration of CNTs as interconnects focuses on vertical interconnects (vias), while growing long-length horizontal CNT interconnects remains challenging. The demonstration of CNT bundle growth in a horizontal direction uses the fact that CNT bundles always tend to grow perpendicular to a surface [80]. However, it requires challenging catalyst deposition techniques and various growth steps to provide a mesh of CNT bundles in two perpendicular directions. Short-length ( $\sim 5 \mu\text{m}$ ) horizontal CNT bundles have been demonstrated in [28] by this approach, as shown in Fig. 8(b), however, the same has not yet been accomplished for long lengths. Controlling the orientation of CNTs by changing the direction of gas flow in the CVD system, horizontal alignment in two dimensions up to millimeter lengths has been achieved for isolated SWCNTs and small number of SWCNTs [81], [82]. However, the substrate needs to be rotated in this approach in order to get a different orientation of the CNTs. Other approaches like electric-field-induced multidirectional growth [83] or fluidic methods [84] are not suited for large-scale integration.

### B. GNR Interconnect Fabrication

While CNTs are difficult to grow in horizontal directions, GNRs are believed to be more fabricable compared to CNTs due to their patternability using lithography. In principle, graphene can be patterned to produce metallic or semiconducting GNRs on demand. Various methods for fabricating GNRs are being pursued, but difficulties also exist in those methods. Carbon films have been demonstrated in DRAM trench capacitors using CVD method [85], but the grown films are not single-crystal graphene with high electrical conductivity. Although the thermal decomposition of single-crystal SiC makes thin graphene films [86], [87], this approach requires single-crystal substrate and high temperature, which is not suitable for interconnects due to the relatively low backend thermal budget ( $\sim 400^\circ\text{C}$ ) in IC fabrication technologies. Graphene can also be mechanically exfoliated from graphite and deposited onto

an insulating substrate [88], but this approach is uncontrollable for large-scale fabrication. In [89], graphene is segregated by dissolving carbon in a Ni substrate at high temperatures, covering with a silicone film, and then transferring to a desired substrate. The Ni substrate can be subsequently removed to allow GNR wire and contact formation through patterning. Similarly, graphene can be deposited on copper foils (which can be removed later) and transferred to insulating substrates [90]. While these approaches are more suitable for interconnect applications than the previous three approaches, they still require further investigation.

To improve the conductivity of multilayer GNRs, intercalation doping has been suggested in [91]. The intercalation doping has been known for a long time in bulk graphite [92]. Generally, graphite can be intercalation doped by exposure to dopant vapor (e.g.,  $\text{AsF}_5$  [92]–[94]). Since multilayer GNRs can be considered as patterned bulk graphite, it is implied that the intercalation doping can be applied to multilayer GNRs.

Most recently, Fujitsu has demonstrated the possibility of building “all carbon” interconnect structures by combining CNTs and GNRs using CVD method [95], where at first, the horizontal GNR layers are grown on a Co film, followed by vertical CNT growth after the Co film has been desegregated to form nanoparticles during the CVD process. However, the contacts between CNT bundle and GNR layers in this structure need more investigation and engineering.

### C. Process Variation

Sustained efforts for developing processes geared toward the large-scale CMOS-compatible fabrication of CNT-based interconnects have yielded promising results. Of particular note are the consistent improvements reported in the fabrication of CNT-based vias compatible with CMOS technologies [28], [29]. However, as expected with all nanoscale technologies, CNT interconnects will also encounter significant process variation challenges. These can arise from several sources—variations in the population of metallic CNTs in a bundle, variations in the diameter and spacing of individual CNTs, contacts to metals, defects along the nanotubes, temperature effects, etc.

While there are some preliminary studies on the impact of process variations in CNT interconnects [96], there is a need for a realistic understanding of the sources of variation, which is in tune with state-of-the-art CNT interconnect fabrication processes. As an example, traditionally used processes for the fabrication of bulk CNT samples exhibit large variations in CNT diameters. However, such processes as arc discharge or laser ablation are clearly not suitable for large-scale integration with CMOS. On the other hand, processes that have been demonstrated as compatible with CMOS interconnects, like low-temperature CVD growth from patterned catalysts, have shown excellent control on parameters such as CNT diameter.

According to [91], many parameters are important from the GNR process variation point of view—wire width and height, edge specularity, doping, defects, etc. However, there is no systematic study on the variation issues of GNR interconnects.

As with any other nanoscale electronic process, controlling manufacturing variations in the fabrication of carbon-based

electronics will be a significant challenge, more so because of fundamental difficulties such as lack of control on chirality. Hence, modeling efforts to comprehend the relevant process variation challenges in CNT and GNR interconnects are as important as developing robust processes that minimize variations. It is instructive to note that while variation-immune/tolerant CNT/GNR interconnect design is desirable, it is important to allow the technology to reach a relatively stable and mature stage for such designs to be impactful.

#### IV. CNT/GNR INTERCONNECT MODELING

##### A. Resistance

The conductance of CNT/GNRs can be derived using the linear response Landauer formula [97]:  $G_n$ , the conductance of the  $n$ th conduction channel (with consideration of spin) in CNT/GNR, can be expressed as

$$G_n = 2e^2/h \cdot \int \tau_n(E)(-\partial f_0/\partial E) dE$$

$$f_0(E) = \{1 + \exp[(E - E_F)/k_B T]\}^{-1} \quad (2)$$

where  $e$  is the elementary charge,  $\tau_n(E)$  is the transmission coefficient,  $f_0(E)$  is the Fermi–Dirac distribution function,  $E_F$  is the Fermi level,  $k_B$  is Boltzmann’s constant, and  $T$  is the temperature. The integration of (2) is from  $|E_n|$  to  $+\infty$  (for electrons) or from  $-\infty$  to  $-|E_n|$  (for holes), where  $E_n$  is the minimum (maximum) energy of the  $n$ th conduction (valence) subband, and can be obtained from the band structure, shown in Fig. 4. The factor of two in the Landauer expression accounts for spin degeneracy (spin up and down), and  $e^2/h$  is the fundamental quantum of conductance. The transmission coefficient  $\tau_n$  can be influenced by defects and interaction with other electrons and phonons.

The total conductance is the sum of conductances of all the conduction and valence subbands. If all modes are assumed to be identical, the Landauer formula (2) can be simplified as

$$G_{\text{total}} = 2e^2/h \cdot M \cdot \tau_{\text{eff}} \quad (3a)$$

$$M = \sum_n [1 + \exp(|E_n - E_F|/k_B T)]^{-1} \quad (3b)$$

where  $G_{\text{total}}$  is the total conductance,  $M$  is the effective number of allowed channels for transport, and  $\tau_{\text{eff}}$  is the effective transmission coefficient.

*Single-Walled CNTs:* For SWCNTs, two bands cross at the Fermi level in the band structure of the metallic  $(n, m) = (7, 7)$  CNT, as can be seen from Fig. 4, therefore  $M = 2$ . Hence, the lowest possible resistance of an isolated SWCNT, assuming perfect metal–CNT contacts ( $\tau_{\text{eff}} = 1$ ), is given by

$$R_Q = \frac{h}{4e^2} = 6.45 \text{ k}\Omega. \quad (4)$$

This is the fundamental quantum of resistance associated with an SWCNT of length less than the MFP ( $\lambda_{\text{CNT}}$ ) of electrons ( $L < \lambda_{\text{CNT}}$ ). For such lengths, electron transport within the nanotube is essentially ballistic, and resistance is independent of length.  $R_Q$  for a CNT is equally divided between the two metal–nanotube contacts (assuming identical contacts) on

either side. However, for lengths  $L > \lambda_{\text{CNT}}$ , scattering leads to an imperfect transmission coefficient [97], i.e.,

$$\tau_n(E) = \left[1 + \frac{L}{\lambda_{\text{CNT}}}\right]^{-1} \quad (5)$$

which yields a total resistance of

$$R = \frac{h}{4e^2} \left(1 + \frac{L}{\lambda_{\text{CNT}}}\right) = R_Q + R_S \cdot L \quad (6a)$$

$$R_S = \frac{h}{4e^2} \cdot \frac{1}{\lambda_{\text{CNT}}} \quad (6b)$$

where  $R_S$  is a distributed resistance per unit length, as shown in (6) (also confirmed by experimental observations [43], [98]).

In this paper, two cases of SWCNT bundle will be considered: one in which all SWCNTs in the bundle are metallic ( $Fm = 1$ ), and another case in which only one-third of the SWCNTs in a bundle are metallic ( $Fm = 1/3$ ), the most natural case [1].

*MFP of CNT:* It can be observed from (6) that the value of MFP plays an important role in determining the resistance of the nanotube. There are several scattering mechanisms for electrons in nanotubes, including acoustic and optical phonon scattering as well as impurity and defect scattering. In general, since different scattering mechanism has different scattering lengths and dependent parameters, the effective MFP of CNTs is a combined effect of all scattering lengths and is dependent on many parameters, such as diameter, voltage bias, length, and temperature. Interestingly, the MFP of these different scattering events are proportional to the diameter due to the averaging out of the effective disorder over the CNT’s diameter, as has been analyzed in [99]–[101]. This is supported by the experimental measurement [44], where ballistic transportation was observed even for the length of 25  $\mu\text{m}$  in large-diameter MWCNTs. For interconnect applications, it has been shown that a low-bias case is valid [102], wherein the acoustic phonon scattering will dominate. In this paper, based on the measurement data in [43], we approximate the electron MFP of a typical SWCNT with  $D = 1 \text{ nm}$  to about 1  $\mu\text{m}$ . Considering its dependence of diameter, we can have

$$\lambda_{\text{CNT}} \approx 1000 D. \quad (7)$$

Note that since this MFP value is extracted from measurement data, it automatically takes into account the presence of any defects in CNTs. Hence, theoretical estimation of MFP (such as in [99] and [100]) will be much larger than this value.

*Multiwalled CNTs:* For multiwalled CNTs (MWCNTs), due to their large diameters, each shell could contribute to the conductance even if it is of semiconducting chirality [65]. In shells with larger diameters, additional states may become populated by thermally activated carriers, because more energy levels are accessible. Thus, MWCNTs almost always show metallic behavior. In this paper, we assume that the diameter of innermost shell is half of the diameter of outermost shell. Therefore, the number of shells ( $p$ ) is given by  $p = 1 + [D_{\text{out}}/4d]$ , where  $D_{\text{out}}$  is the diameter of outermost shell in a MWCNT,  $d$  is the distance between adjacent shells ( $= 0.34 \text{ nm}$ ), and  $[\cdot]$  above indicates that only the integral part is taken into account. For

a shell with diameter ( $D$ ), the number of conducting channels of that shell in an MWCNT can be calculated using (3b) and is approximated as in [103]

$$M_{\text{shell}}(D) \approx a \cdot D + b, \quad D > 3 \text{ nm} \quad (8)$$

where  $a = 0.0612 \text{ nm}^{-1}$ , and  $b = 0.425$ . Note that the assumption under (8) is that shells in an MWCNT have a one-third probability of having a metallic chirality and a two-thirds probability of having a semiconducting chirality. In addition to the number of conducting channels, the MFP of each MWCNT shell is also different and can be calculated using (7). Using (7) and (8) in (3), the total conductance of MWCNT can be calculated [65], [103]. It should be noted that the individual shells in an MWCNT will be perturbed by adjacent shells. However, these adjacent shells are likely to have different chiralities that produce near random perturbations that fluctuate on a scale that is small with respect to the nanotube diameter [55]. Hence, it can be assumed that the electrical properties of each shell in an MWCNT will be retained, but there are resistive, capacitive, and inductive interactions among the shells, as shown in [65].

**Double-Walled CNTs:** Although DWCNTs are constructed from two SWCNTs with the same or different chiralities, the electronic properties of each nanotube within a DWCNT can be different from those of an isolated SWCNT. Semiconducting shells in a DWCNT may behave as metallic [104], as a result of charge transfer and orbital mixing [105]. In this paper, we consider the ideal case where both the inner and outer shells of a DWCNT are metallic. For this ideal case, each DWCNT has conducting channels  $M = 4$ .

**Monolayer GNR:** According to the simple tight binding model (linear approximation near the Dirac point), the minimum (maximum) energy of the  $n$ th conduction (valence) subband  $|E_n|$  [see Fig. 4(b)] can be approximately calculated for zz-GNRs [106] as follows:

$$E_0 = 0 \quad (9a)$$

$$|E_n| = (|n| + 1/2) \cdot hv_F/2w \text{ for } n \neq 0 \quad (9b)$$

where  $v_F = 10^6 \text{ m/s}$  is the Fermi velocity, and  $w$  is the width of the GNR. A zero bandgap of zz-GNRs is assumed in (9a). However, in reality, a bandgap is induced because of the staggered sublattice potential from magnetic ordering once electron spin is considered when the width of zz-GNRs is small enough [19], [59]. The bandgap of zz-GNRs increases with decreasing wire width (the bandgap in electronvolts is  $0.933/(w + 1.5)$  with  $w$  in nm). In such situation, (9a) can be modified as

$$E_0 = \frac{0.933}{2(w + 1.5)}. \quad (9c)$$

The transmission coefficient  $\tau_n(E)$  in (2) is determined by both edge scattering and scattering by defects and phonons. The edge scattering is schematically shown in Fig. 9, where  $\cot \theta$  is the ratio of longitudinal (along the wire length) to transverse (across the wire width) velocities, and  $\theta$  can be calculated from  $|\sin \theta| = |E_n/E|$  [107]. If complete diffusive edge is assumed, transmission coefficient due to edge scattering can be expressed by “ $w \cot \theta/L$ ,” where  $w \cot \theta$  is the average distance that electrons/holes travel before hitting the edge, and

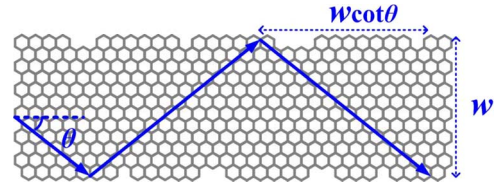


Fig. 9. Schematic view of edge scattering in GNRs and the definition of  $\theta$ . The width of the GNR is  $w$  and  $w \cot \theta$  is the average distance that electrons/holes travel before hitting the edge. Note that  $L/(w \cot \theta)$  and  $L/(\lambda_{\text{GNR}} \cos \theta)$  represent the number of scattering events due to edge scattering and defect scattering, respectively.  $\lambda_{\text{GNR}}$  is defined along the electron/hole transport direction (indicated by the solid arrows).

$L$  is the length of the GNR. On the other hand, due to scatterings by defects and phonons (not edge scattering), the transmission coefficient can be expressed by “ $\lambda_{\text{GNR}} \cos \theta/L$ ,” where  $\lambda_{\text{GNR}}$  is the MFP corresponding to such scattering.  $\lambda_{\text{GNR}} \cos \theta$  represents the average distance that electrons/holes travel along the GNR longitudinal direction before collision. Hence, if complete diffusive edge is assumed, using the Matthiessen’s rule,  $\tau_n(E)$  can be expressed as [107]

$$\tau_n(E) = \left( 1 + \frac{L}{\lambda_{\text{GNR}} \cos \theta} + \frac{L}{w \cot \theta} \right)^{-1}. \quad (10)$$

If the edge specularity is considered, the second term in (10) needs to be modified, and the effective transmission coefficient  $\tau_n(E)$  now should be [107]

$$\tau_n(E) = \left[ 1 + L \left( \frac{1}{\lambda_{\text{GNR}} \cos \theta} + \frac{1-p}{w \cot \theta} \right) \right]^{-1} \quad (11)$$

where  $p$  is the edge specularity. The conductance model for ac-GNRs is complicated. Theoretical analysis indicates that ac-GNRs can be differentiated as metallic and semiconducting, but this is not valid from a practical point of view [108], since nanopatterning down to the accuracy of one atom is a formidable task. Although there are reports that graphene can be cut along certain crystallographic directions and potentially produce armchair or zigzag GNRs with smooth edges using nanoparticles [109], this approach is not controllable: neither the diameter of the particles (which implies the slot width) nor the moving direction of the particles (which implies the slot direction) can be accurately controlled. Since the band structure of ac-GNRs changes dramatically (from semiconducting to metallic) with width variation, even at the atomic scale, the modeling of ac-GNR interconnect requires careful consideration. In this paper, we will only consider zz-GNRs for interconnects, where small variation of width will not induce significant change in the band structure.

**MFP of GNR:** From (11), it is obvious that  $\lambda_{\text{GNR}}$  plays an important role in determining the conductance of GNRs. Similar to CNTs,  $\lambda_{\text{GNR}}$  of a monolayer GNR is proportional to its width ( $w$ ) [91], [108], theoretically, we have

$$\lambda_{\text{GNR}} \approx \frac{2w}{\sqrt{3}} \cdot \frac{\gamma^2 - E^2/4}{\sigma_\varepsilon^2 + 4\sigma_\gamma^2} \approx \frac{4w}{\sqrt{3}} \cdot \frac{\gamma^2}{2\sigma_\varepsilon^2 + 8\sigma_\gamma^2} \quad (12)$$

where  $\sigma_\varepsilon$  and  $\sigma_\gamma$  are the variances of different Hamiltonian matrix elements [99],  $\gamma = -2.7 \text{ eV}$ , and  $E$  is the energy measured

with respect to  $E_F$ . Comparing (7) and (12),  $\lambda_{\text{GNR}}$  (monolayer) can be approximately expressed as

$$\lambda_{\text{GNR}} \approx 450w. \quad (13)$$

In reality, the experimental  $\lambda_{\text{GNR}}$  value ( $\sim 1 \mu\text{m}$ ) [45], [86], is much smaller than that predicted by (13), as long as the width is not too small, which is due to the scattering from defects and is width independent. However, this is not a physical limit and can be improved as fabrication technology progresses. In the following analysis, an optimistic but arbitrary value of  $\lambda_{\text{GNR}} = 5 \mu\text{m}$  is assumed for monolayer GNRs. It will be shown that even with this optimistic MFP, monolayer GNRs cannot match the performance of Cu interconnects.

**Multilayer GNR:** To improve the total conductance, multilayer GNRs are needed. However, when graphene layers are stacked together (typically, ABAB stacking), the MFP and conductance per layer is reduced because of intersheet electron hopping [110]. The MFP of neutral multilayer GNR (graphite) is extracted as 419 nm [107] from the in-plane conductivity of  $0.026 (\mu\Omega \cdot \text{cm})^{-1}$  [110]. The in-plane conductivity of graphite can be increased by several tens of magnitude by intercalation doping, because doping can increase the carrier density due to charge transfer and increase the MFP due to increased layer spacing (interlayer scattering is suppressed) [92]. For example, the stage 2  $\text{AsF}_5$  intercalated graphite can have in-plane conductivity of  $0.63 (\mu\Omega \cdot \text{cm})^{-1}$ , which is slightly greater than the bulk conductivity of Cu. According to [107],  $|E_F| = 0.60 \text{ eV}$  and the MFP for stage 2  $\text{AsF}_5$  intercalation-doped GNR is  $\lambda_{\text{GNR}} = 1.03 \mu\text{m}$ .

It should be noted that there is report that the adjacent layers do not interact with each other in multilayer GNRs grown on C-faced 4H-SiC (000 $\bar{1}$ ) [87], [111]. However, this type of multilayer GNRs is an unlikely candidate for interconnect applications due to two reasons: 1) Interconnect wires are fabricated on top of dielectrics, but not single-crystal SiC and 2) adjacent layers are rotated by  $30^\circ \pm 2.204^\circ$ , which implies that if the first GNR layer is zigzag edge, the second layer becomes approximately armchair edge, and there is no report of how to perform intercalation doping in such GNRs, which would imply low conductance.

**Resistance Comparison:** Fig. 10 shows the resistance comparison for different types of CNT and GNR interconnects. The dimension of interconnects is adapted from the International Technology Roadmap for Semiconductors (ITRS) 2008 [112] prediction for local interconnects for both 14- and 22-nm technology nodes. For DWCNT, the diameter is set to be 1.5 nm. The outmost diameter of MWCNTs and the width of all GNRs are set to be equal to the wire width ( $W$ ). It can be observed that for all types of CNTs and GNRs, their resistances decrease with increasing length and become stable after  $10 \mu\text{m}$  (MWCNTs require longer length to stabilize since they have longer MFP). For wire lengths  $> 10 \mu\text{m}$ , all types of CNTs could offer lower resistance than Cu, whereas only  $\text{AsF}_5$  intercalation-doped GNRs with high edge-specularity can provide a resistance lower than that of Cu. Note that the resistance of monolayer GNR with  $p = 0.41$  is too high and out of range in Fig. 10. The resistance comparison shown in Fig. 10 provides insight into

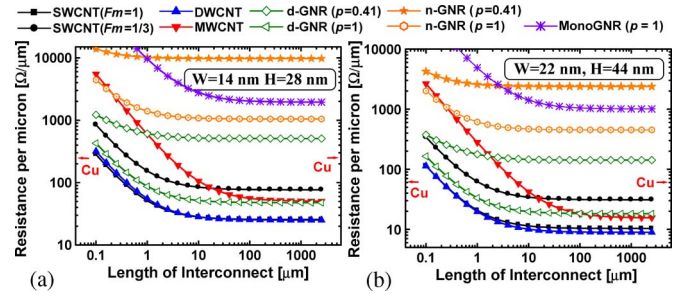


Fig. 10. Resistance per unit length comparison for different types of CNT and GNR interconnects. For DWCNT, the diameter is set to be 1.5 nm, and the metallic fraction  $Fm = 1$ . The diameter of MWCNT and the width of GNR are equal to the wire width ( $W$ ). n-GNR and d-GNR represent neutral multilayer GNRs and  $\text{AsF}_5$  intercalation-doped multilayer GNRs, respectively.  $p$  is the edge specularity.

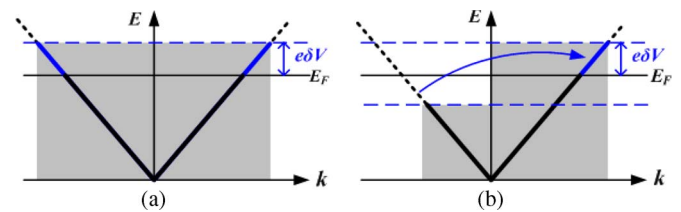


Fig. 11. Electron energy versus wave vector ( $k$ ) in CNT/GNR 1-D material with low density of states. Equilibrium state (a) after adding charges and (b) after a current has been established.  $E_F$  is the Fermi energy. The dotted line represents available states, and the solid line or shadowed area represents occupied states. In (b), electrons move to the right in the area where  $\partial E/\partial k > 0$  and to the left in the area where  $\partial E/\partial k < 0$ . In order to establish a net current from right to left, the number of electrons moving to the right must exceed that moving to the left.

the performance of CNT and GNR interconnects vis-à-vis Cu wire (discussed in more detail in Section V-A).

### B. Capacitance

An external voltage applied to a 1-D conductor affects its electrochemical potential energy in two ways. The change in electrostatic potential energy when a charge  $\delta Q$  is added to the conductor is given by  $(\delta Q)^2/(2C_E)$ , where  $C_E$  is its *electrostatic capacitance*, which is the traditional capacitance. In addition, due to the low density of states at the Fermi energy level, the charge  $\delta Q$  has to occupy available quantum energy states above the Fermi energy level as shown in Fig. 11(a). Since the density of states of CNT/GNR is low, the energy required to occupy higher states is high and cannot be ignored. Assuming that the additional quantum energy required to add charge  $\delta Q$  to these higher energy states is  $e\delta V$ , following traditional capacitance definition, *quantum capacitance* can be modeled as [113]–[116]:

$$C_Q = \frac{\delta Q}{\delta V}. \quad (14)$$

Hence, the net change in electrochemical potential energy is given by

$$\delta E = \frac{(\delta Q)^2}{2C_E} + \frac{(\delta Q)^2}{2C_Q} = \frac{(\delta Q)^2}{2C_{\text{total}}} \quad (15)$$

where  $C_{\text{total}}$  is the total effective capacitance of a 1-D conductor. From (15), it can be deduced that  $C_{\text{total}}$  is given by a

TABLE III  
ITRS-2008-BASED SIMULATION PARAMETERS

Technology Node (nm)		22	14
Local (driver size: 2)	Width $W$ (nm)	22	14
	Height $H$ (nm)	44	28
	ILD Thickness (nm)	39.6	25.2
	$\rho_{Cu}$ ( $\mu\Omega\cdot cm$ )	6.01	8.19
	$C_{Cu}$ (pF/m)**	131.01	111.83
	$C_{MWCNT}$ (pF/m)**	117.70	100.51
Intermediate (driver size: 20)	Width $W$ (nm)	44	28
	Height $H$ (nm)	44	28
	ILD Thickness (nm)	39.6	25.2
	$\rho_{Cu}$ ( $\mu\Omega\cdot cm$ )*	4.235	5.386
	$C_{Cu}$ (pF/m)**	115.67	98.75
	$C_{MWCNT}$ (pF/m)**	100.0	89.57
Global (driver size: 100)	Width $W$ (nm)	160	105
	Height $H$ (nm)	96	63
	ILD Thickness (nm)	76.8	52.5
	$\rho_{Cu}$ ( $\mu\Omega\cdot cm$ )*	2.942	3.294
	$C_{Cu}$ (pF/m)**	143.02	118.98
	$C_{MWCNT}$ (pF/m)**	135.5	111.01
Minimum Sized Gate	$R_t$ (K $\Omega$ )	29.236	35.288
	$C_{in}$ (aF)	45.514	21.84
	$K_{ILD}$	2.05	1.75

\* Calculated using the model in [50] to capture the size effect of Cu wire.

\*\* These capacitances are calculated using an FEM tool [118].

series combination of  $C_E$  and  $C_Q$ . The quantum capacitance  $C_Q$  depends on the density of states at the Fermi energy level  $D(\mu)$ . For each channel, it is given by [113]–[116]

$$C_{Q/channel} = \frac{1}{2}e^2 D(\mu) = \frac{2e^2}{\pi \hbar v_F} = \frac{4e^2}{\hbar v_F} \sim 193 \text{ aF}/\mu\text{m}. \quad (16)$$

For metallic SWCNTs, there are two conducting channels, while for MWCNTs and GNRs, the channel number can be calculated using (3b). Note that the value of (16) is in the same order as typical electrostatic capacitance (will be shown in Table III), therefore, for a small number of CNTs,  $C_Q$  should not be ignored. For conventional 3-D conductors, the density of states  $D(\mu)$  is very large, hence,  $C_Q$  is large and its effect on overall capacitance is negligible.

Electrostatic capacitance of CNT will depend on the geometry of the structure. For a bundle structure, it also depends on the bundle density. As shown in [102] and [117], the most densely packed SWCNT bundle has slightly smaller capacitance compared to that of a Cu wire. As density decreases, the capacitance of CNT bundle decreases slowly. In this paper, the electrostatic capacitance of SWCNT bundle is assumed to be equal to that of Cu wire, which can be regarded as an upperbound of electrostatic capacitance for dense SWCNT bundles. Similarly, electrostatic capacitance of multilayer GNR is assumed to be equal to that of Cu wire. For MWCNTs and monolayer GNRs, the electrostatic capacitance is calculated by a finite-element method (FEM) tool [118]. Note that the capacitance of the MWCNTs cannot be assumed to be equal to that of the corresponding Cu wire, due to non-negligible fringing effects arising from the smaller number of MWCNTs in the bundle.

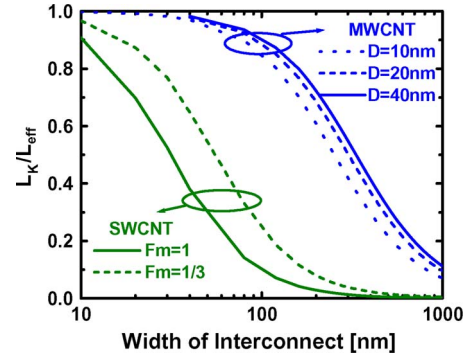


Fig. 12. Ratio of kinetic inductance and total effective inductance of SWCNT (with different metallic fractions  $F_m$ ) and MWCNT (with different diameters) bundles as a function of interconnect width. The interconnect height is set equal to the width, and the interconnect length is 500  $\mu\text{m}$ .

### C. Inductance

The inductance of a conductor models the energy associated with the motion of electrons carrying current ( $I$ ) through it. The energy stored in the magnetic field generated by the current is given by  $(1/2)L_M I^2$ , where  $L_M$  is its *magnetic inductance*. For a net current  $\delta I$  to flow through a conductor, there has to be an excess of electrons moving in the direction opposite to current flow. Fig. 11(b) shows that there are more right moving electrons (in the region  $\partial E/\partial k > 0$ ) than left moving electrons (in the region  $\partial E/\partial k < 0$ ) in order to establish a net current (from right to left). In a 1-D conductor that has low density of states at the Fermi energy level ( $E_F$ ), these right-moving electrons can only be added at available quantum energy states above  $E_F$  and, thus, have a higher kinetic energy than those left-moving electrons, as shown in Fig. 11(b). This kinetic energy, stored in the moving electrons responsible for current flow in a 1-D conductor, is modeled as

$$\delta E = \frac{1}{2}L_K \delta I^2 \quad (17)$$

where  $L_K$  is its *kinetic inductance*. The net change in energy due to current flow in the conductor is given by

$$\delta E = \frac{1}{2}L_K \delta I^2 + \frac{1}{2}L_M \delta I^2 = \frac{1}{2}L_{\text{total}} \delta I^2 \quad (18)$$

where  $L_{\text{total}}$  is the total effective inductance of a 1-D conductor. From (18), it can be deduced that  $L_{\text{total}}$  is given by a series combination of  $L_M$  and  $L_K$ .

For a 1-D conductor, the kinetic inductance per channel is given by [113]–[116], [119]

$$L_{K/channel} = \frac{\hbar}{4e^2 v_F} = 8 \text{ nH}/\mu\text{m} \quad (19)$$

and it scales with the number of conducting channels. This theoretical value of kinetic inductance is in agreement with experimental observations in [120].

The fraction of kinetic inductance in the total inductance of CNT interconnects for different cross sections has been analyzed in [31] and shown in Fig. 12. As can be observed, kinetic inductance forms a significant fraction of the total inductance when the width of SWCNT interconnects is smaller than

100 nm. However, it becomes much more significant in case of MWCNT bundles. This is because the number of conducting channels in a MWCNT bundle is small compared to that of SWCNT bundles for a given cross section [65], and  $L_K$  scales down linearly with number of conducting channels.

#### D. High-Frequency Analysis of CNT/GNR Interconnect

From traditional analysis of 3-D metal conductors, it is well known that the resistance and inductance of interconnects are strongly dependent on the frequency due to skin effect and/or proximity effect. At high frequencies, the resistance of a metal wire increases significantly while inductance decreases with the frequency. To understand the high-frequency behavior of CNT interconnects, extracting frequency-dependent resistance and inductance of CNT interconnect is the critical step [31]. For the CNT interconnect bundle structure, each CNT in the bundle would have self-impedance and mutual impedance as follows:

$$Z_{\text{self}} = R_{\text{CNT}} + j\omega(L_{\text{kinetic}} + L_{\text{self}}) \quad (20)$$

$$Z_{\text{mutual}} = j\omega M \quad (21)$$

where  $\omega$  is the frequency,  $R_{\text{CNT}}$  is the resistance of each CNT including quantum and scattering resistance (6), and  $L_{\text{kinetic}}$  is the kinetic inductance of CNT.  $L_{\text{self}}$  and  $M$  are magnetic self-inductance and mutual inductance of CNT, respectively. Note that the self-impedance of each CNT consists of resistive and inductive (both kinetic and magnetic) impedance. However, mutual impedance (21) only consists of magnetic mutual inductive impedance since there is no mutual resistance and mutual kinetic inductance. The intertube resistance between CNTs in a bundle has been shown to be on the order of megaohms [98] and can be ignored.  $L_{\text{self}}$  and  $M$  can be obtained by employing the concept of *geometric mean distance (GMD)* and *arithmetic mean distance (AMD)* [121]. The detailed equations for CNTs can be found in [31]. Therefore, for a CNT bundle, its impedance matrix is given as

$$[Z_{\text{matrix}}] = \begin{bmatrix} Z_{\text{self}}^1 & j\omega M^{21} & \dots & j\omega M^{n1} \\ j\omega M^{21} & Z_{\text{self}}^2 & \dots & j\omega M^{n2} \\ \vdots & \vdots & \ddots & \vdots \\ j\omega M^{n1} & j\omega M^{n2} & \dots & Z_{\text{self}}^n \end{bmatrix}. \quad (22)$$

Having this impedance matrix, the effective total impedance of the bundle can be obtained for a given frequency  $\omega$  by solving the matrix equation  $[V] = [Z][I]$ , where the current vector  $[I]$  can be extracted for a given voltage  $V_0$  across the bundle. The effective total impedance can be obtained by

$$Z_{\text{eff}} = V_0 / \text{sum}[I] \quad (23)$$

where  $\text{sum}[I]$  is the sum of the current in each CNTs in the bundle for voltage  $V_0$ . Therefore, the total effective resistance and inductance can be obtained as

$$R_{\text{eff}} = \text{real}(Z_{\text{eff}}) \quad (24a)$$

$$\omega L_{\text{eff}} = \text{imag}(Z_{\text{eff}}). \quad (24b)$$

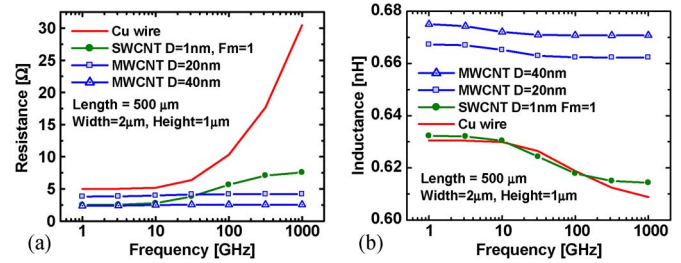


Fig. 13. Total effective (a) resistance and (b) inductance of SWCNT and MWCNT bundles with different diameters as a function of frequency, compared with identical cross section Cu wires.

Fig. 13 shows the total effective resistance and inductance values of CNT interconnect as a function of frequency as compared with a Cu wire. The resistance and inductance of Cu wire are extracted by FastHenry [122]. It can be observed that the resistance of Cu wires increases dramatically, while the inductance decreases in the high-frequency region due to significant skin effect that reduces the effective area of current return loops. However, it is interesting to observe that the resistance and inductance of CNT bundle saturate at high frequencies. Particularly for MWCNTs, their resistance almost remains unchanged, implying a negligible skin effect.

The reduced skin effect of CNT bundle can be attributed to the presence of large kinetic inductance. Due to the existence of kinetic inductance ( $= \tau/\sigma_0$ ), the resistivity of CNT bundle becomes complex and can be written as [119]

$$\rho(\omega) = \frac{1 + j\omega\tau}{\sigma_0} = \frac{1}{\sigma_0} + j\omega \frac{\tau}{\sigma_0} \quad (25a)$$

$$\tau = \lambda/2v_F \quad (25b)$$

where  $\sigma_0$  is the frequency-independent dc conductivity [obtained from (2) or (3)],  $\tau$  is the momentum relaxation time,  $\lambda$  is the MFP of CNTs. The second term of (25a) is the impedance due to kinetic inductance. Based on this complex conductivity, one can derive the equivalent skin depth of a CNT bundle as [119]

$$\delta = \sqrt{\frac{2}{\omega\mu\sigma_0}} \cdot \sqrt{[(\omega\tau)^2 + 1] \cdot [\sqrt{(\omega\tau)^2 + 1} - \omega\tau]} \quad (26)$$

where the first term is the classical skin depth and  $\mu$  is the permeability of the material. For the case of conventional metals (typically  $\tau$  is very small or  $\omega\tau \ll 1$ ), (26) reduces to the classical skin depth. The equivalent skin depth of CNT bundles has been calculated as shown in Fig. 14(a) [119]. It can be observed that the skin depth of Cu wire continues to reduce with frequency, whereas the skin depths of CNTs saturate after certain frequencies due to existence of large kinetic inductance or large momentum relaxation time  $\tau$ . The value of this saturation frequency will depend on the momentum relaxation time  $\tau$ . CNTs with larger diameters have larger  $\tau$  values and will saturate earlier. It is interesting to find that MWCNTs will not only start saturating at a relatively lower frequency but will also have relatively large saturated skin depths. Considering the fact that MWCNTs could have comparable circuit

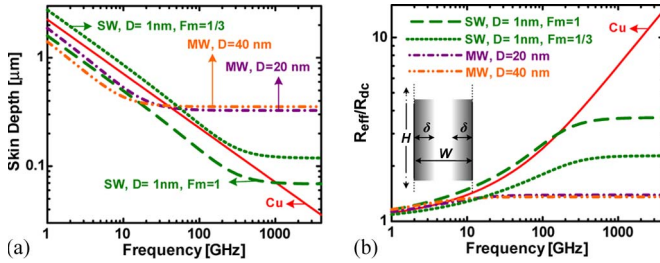


Fig. 14. (a) Skin depth of different types of CNT materials as well as Cu as a function of frequency. (b) Ratio of high-frequency resistance with respect to the dc resistance for different types of CNT materials and Cu [119].

performance to that of SWCNTs [65], it can be expected that MWCNTs would have significant advantages in high-frequency applications.

We further evaluate the high-frequency resistance for the semi-infinite structure shown in the inset of Fig. 14(b), where the width of conductor is  $W$  and the height is infinite so that we will only consider the skin effect along the width. The high-frequency resistance of this semiinfinite structure can be calculated (detailed equations can be found in [119]) and its ratio with respect to dc resistance is shown in Fig. 14(b) for  $W = 1 \mu\text{m}$ . It can be observed that the resistance of Cu increases dramatically at high frequencies, whereas the resistance of CNTs saturate at high frequencies. Particularly, MWCNTs exhibit only a small increase ( $< 9\%$ ). Also, SWCNTs with  $Fm = 1$  exhibit greater increase in resistance (w.r.t. SWCNTs with  $Fm = 1/3$ ) due to larger  $\sigma_0$  or smaller effective kinetic inductance [from (25)].

It should be noted that for traditional metals, we cannot observe this frequency saturation effect due to the fact that the kinetic inductance is too small in conventional metals. This is due to two reasons. First, the momentum relaxation time for a metal is usually very small (on the order of  $10^{-14}$  s) [123], and thus, the imaginary part of (25a) is negligible for frequencies less than a terahertz ( $\omega\tau \ll 1$ ). Moreover, the total kinetic inductance also scales down with the number of conducting channels  $M$ , which is usually very large for metals, unless for very small dimensions. Whereas, the momentum relaxation time for a CNT is on the order of  $10^{-12}$  s, or even larger ( $\omega\tau \sim 1$ ), and the  $M$  for a CNT is small ( $= 2$  for a SWCNT). Hence, one can observe a significantly large kinetic inductance in CNTs. The above skin effect analysis of CNT material is in agreement with our impedance extraction results shown in Fig. 13.

From the above analysis, it can be concluded that the large kinetic inductance in CNTs has two effects. The first one is that it increases the overall inductance value. However, this increment becomes small (particularly for SWCNTs) for large bundle size due to the fact that total kinetic inductance scales down with the number of channels or number of tubes. This can be observed in Fig. 12. The second effect is more subtle and only becomes significant in the high-frequency region, which leads to the reduced skin effect in CNT bundles as has been discussed in this section.

The unique high-frequency behavior of CNT interconnect is very promising for high-frequency applications since one of the important issues in high-frequency circuit design is that the

conductor loss increases dramatically due to skin effect. Since the resistance of CNT interconnects increases by a smaller amount or remains almost unchanged at high frequencies, the high-frequency performance of the circuit can be enhanced significantly by employing CNT interconnects.

The high-frequency effect in multilayer GNRs is much more complicated than in CNTs as well as in traditional metals (Cu). Treating each GNR layer as one element is not valid in high-frequency analysis. Typically, the CNT diameter ( $< 40$  nm) is much smaller than its classical skin depth (defined as  $\delta_{\text{CSE}} = \sqrt{2\rho_{\text{eff}}/\mu\omega}$  [124] where  $\rho_{\text{eff}}$  is the effective resistivity) when frequency is below 100 GHz. However, for the case of GNR, the width of the GNR layers (which equal the width of the wires) can be larger than the classical skin depth. Hence, there should be some current density redistribution within a GNR layer. Furthermore, treating multilayer GNRs as a traditional metal is not valid either. The MFP of traditional metal (Cu) is 40 nm at room temperature, which is much smaller than its classical skin depth when frequency is below 100 GHz. The MFP of GNR, however, is on the order of  $1 \mu\text{m}$ , which can be larger than its classical skin depth. In such case, an anomalous skin effect arises [124], which requires solving the Boltzmann equation rather than using Ohm's law for conductance calculation. Quantitative analysis is required in the future to accurately estimate the skin effect in GNRs.

### E. Thermal Modeling of CNTs

Almost all works analyzing the applicability of CNT interconnects in VLSI circuits [64], [65], [117], have only addressed their electrical performance in terms of providing low-latency horizontal paths on a chip, except some initial analysis in [102], [125] but no thermal model was provided.

As mentioned in Section II-C, phonons dominate thermal transport in CNTs. The thermal conductance ( $G_{\text{CNT}}^{\text{thermal}}$ ) due to phonons in a CNT can be calculated as [126]

$$G_{\text{CNT}}^{\text{thermal}} = \sum_{n, v_n > 0} \int \frac{dq}{2\pi} \hbar \omega_n(q) v_n(q) \frac{\partial f}{\partial T} \tau_n(q, \omega_n) \quad (27a)$$

$$v_n(q) = \frac{\partial \omega_n(q)}{\partial q} \quad (27b)$$

$$f = 1/[e^{\hbar\omega_n/k_B T} - 1] \quad (27c)$$

where  $\omega_n(q)$  is the phonon dispersion, which can be calculated following the methodology in [127],  $\tau_n(q, \omega_n)$  is the energy transmission coefficient for the  $n$ th phonon branch wave at longitudinal momentum  $q$ ,  $f$  is the Bose-Einstein distribution function, and  $v_n(q)$  is the group velocity along the direction of thermal transport. The integration over momentum  $q$  is within the first Brillouin zone. The central problem in solving (27) is to find out the transmission coefficient  $\tau_n(q, \omega_n)$ , which will depend on the phonon scattering.

Similar to electrical transport, for the ballistic region, where the CNT length is smaller than phonon MFP  $\lambda_{\text{ph}}$ , the transmission coefficient  $\tau_n$  can be assumed to be 1. Several experimental analyses have demonstrated evidence of ballistic thermal transport in CNTs. SWCNTs with diameters between 1 and

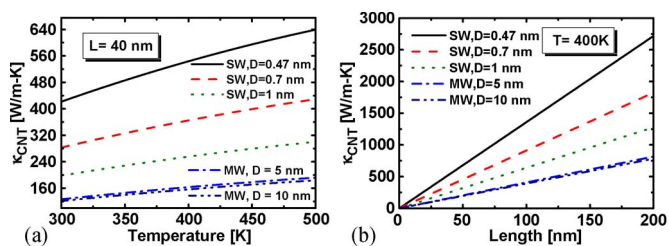


Fig. 15. Equivalent thermal conductivity ( $\kappa_{\text{CNT}}$ ) for isolated thermally ballistic CNTs of different diameters as a function of (a) temperature and (b) length.

3 nm have shown ballistic thermal conductance for lengths larger than  $2 \mu\text{m}$  at room temperature [36]. MWCNTs with a diameter of 14 nm have also shown large phonon MFPs ( $\sim 500 \text{ nm}$ ) at 320 K [37]. Thermal conductance of ballistic CNTs can be calculated by (27) and the equivalent thermal conductivity ( $\kappa_{\text{CNT}} = G_{\text{CNT}}^{\text{thermal}} \cdot L/A$ , where  $A$  is the area occupied by a CNT) is shown in Fig. 15 [128]. It is shown that  $\kappa_{\text{CNT}}$  of isolated CNTs depends on their diameter, length, and temperature. Ballistic thermal conductivity of CNTs increases with temperature because higher temperature will populate more phonon modes. Moreover, the thermal conductivity decreases with the diameter due to the fact that large diameter SWCNT occupies larger area  $A$ , but this effect is not obvious for MWCNTs because larger diameter MWCNTs have more shells (and thus larger thermal conductance) to counterbalance the effect of area increase. For thermally ballistic CNTs, since the conductance is a constant for a given diameter CNT, larger length also indicates higher equivalent thermal conductivity, as shown in Fig. 15(b). The large values of  $\kappa_{\text{CNT}}$  exceeding  $1000 \text{ W/m} \cdot \text{K}$  are shown to be achievable for isolated CNTs for lengths exceeding 100 nm and very small diameters.

For quasi-ballistic ( $L \sim \lambda_{\text{ph}}$ ) or diffusive region ( $L > \lambda_{\text{ph}}$ ), the thermal conductivity ( $\kappa_{\text{CNT}}$ ) of CNT will depend on the length, temperature, and MFP, unless  $L \gg \lambda_{\text{ph}}$  where it can be regarded as length independent. Recent molecular dynamics simulations [129] as well as theoretical analysis [130] show that the thermal conductivity of SWCNT follows a power law ( $\kappa_{\text{CNT}} \propto L^a$ ), where  $0 < a < 1$  dependent on length if it is in the quasi-ballistic region. This indicates that  $\kappa_{\text{CNT}}$  will keep increasing with the length even in quasi-ballistic region, and will eventually become length independent for long lengths. Hence, if CNT based through-silicon vias (that are tens of microns in height), are employed in 3-D ICs, they will have significant advantage due to higher thermal conductivity than any other metals. However, the model for exponent  $a$  is still not determined and cannot be used in the general case. In [126], the transmission coefficient  $\tau_n(q, \omega_n)$  in quasi-ballistic region is modeled by

$$\tau_n(q, \omega_n) = \frac{\lambda_{\text{ph}}(\omega)}{\lambda_{\text{ph}}(\omega) + L}. \quad (28)$$

This approximation could also lead to thermal conductivity as a power law dependent on length. However, the determination of phonon MFP is not well known. Several works in the published literature express the inability to accurately predict the phonon MFP in CNTs [36], [126].

For thermal modeling of CNT, understanding the phonon scattering mechanism is very critical. Unfortunately, this mechanism is not well understood yet. For quasi-ballistic region, the dominant mechanism is expected to be Umklapp phonon-phonon scattering. While for longer lengths, second or higher order three-phonon scattering processes should be considered [131], [132]. To fully understand the phonon scattering mechanisms in CNTs, more experimental and theoretical work is required in the future.

## V. APPLICATIONS

The physics and properties of CNTs have been studied for nearly two decades, and many possible applications for these nanomaterials have already been widely explored. However, active research into graphene and its derivatives is a more recent development and a lot more work is needed to gauge the true potential of GNRs. Here, we address several applications for CNTs related to interconnects and passives, alongside GNR-based interconnects that have recently been proposed.

### A. CNT/GNR Interconnect

There have been several works focusing on the circuit modeling of CNT interconnects. A simple circuit model was presented in [113] for metallic SWCNT by using the Luttinger liquid theory [114], which explicitly separates the spin mode (does not carry charge current) and the charge mode (carries charge current), providing insightful understanding of electron transport in SWCNTs. By adding a distributed scattering resistance term to the model in [113], an *RLC* equivalent circuit for SWCNTs has been proposed in [64], [102], and [117], as shown in Fig. 16(a). Subsequently, the equivalent circuit model for MWCNTs (also applicable to DWCNTs) has been proposed in [65] and shown in Fig. 16(b).

It should be noted that since the spin mode does not carry charge current, an identical CNT circuit model can also be derived using different approaches by only considering the charge mode and without involving the Luttinger liquid theory, such as those based on the semiclassical Boltzmann transport equation [116], the Fluid model [133],<sup>1</sup> or an electron waveguide transmission-line analog [134], [135]. Recently, a similar equivalent circuit model for monolayer or multilayer GNRs has also been proposed, albeit with different conductance calculation methods [91], [106].

The equivalent circuit model [Fig. 16(b)] for MWCNTs is different from that of a SWCNT due to the fact that different shells have different RLC parameters and there are interactions between shells. Therefore, DWCNT or MWCNT is modeled as two or more parallel RLC lines, respectively. Each RLC line is similar to the one shown in Fig. 16(a) and represents one shell. The details of the model for MWCNT (also valid for DWCNT) interconnect can be found in [65]. Having the equivalent circuits for different carbon-nanomaterial-based interconnects as shown in Fig. 16, their performance can be analyzed using SPICE simulations and compared to that of a Cu wire. All

<sup>1</sup>Considers electrostatic potential as the output voltage, while other works (including this work) consider electrochemical potential as the output.

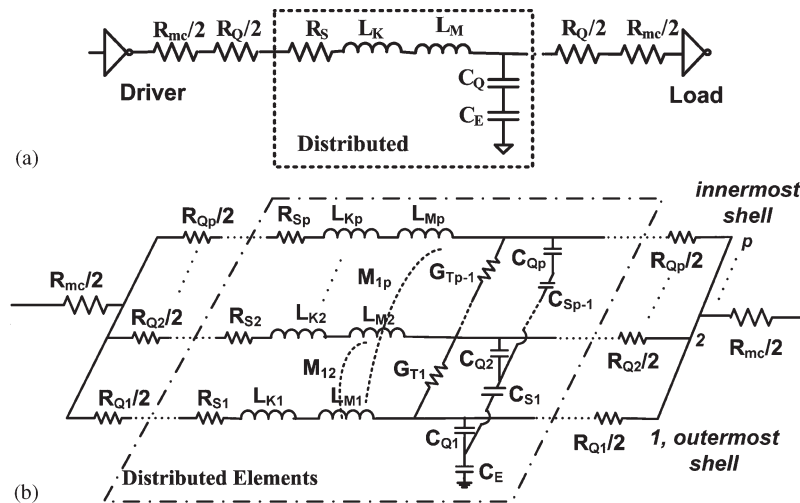


Fig. 16. Equivalent distributed circuit model of (a) an SWCNT or a GNR interconnect and (b) an MWCNT interconnect with  $p$  shells.  $R_{mc}$  is the imperfect contact resistance;  $R_Q$  is the quantum contact resistance;  $R_S$  is the scattering-induced resistance;  $L_K$  and  $L_M$  are the kinetic inductance and magnetic inductance associated with CNTs or GNRs, respectively;  $M$  is the mutual inductance among MWCNT shells; and  $C_Q$  and  $C_E$  are the quantum capacitance and electrostatic capacitance, respectively. Note that, in (b), the shell-to-shell capacitance  $C_S$  and the tunneling conductance  $G_T$  only have  $p - 1$  distributed components.

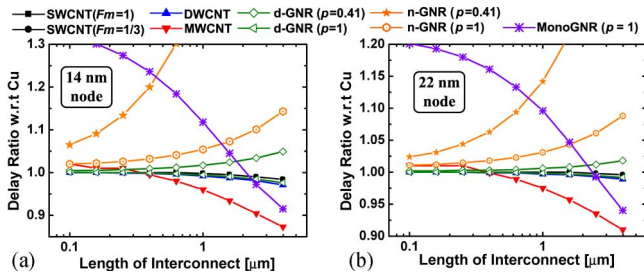


Fig. 17. Signal delay ratios (with respect to Cu) of SWCNT, DWCNT, MWCNT, and different types of GNRs at the local interconnect level for the (a) 14-nm and (b) 22-nm technology nodes.  $F_m$  indicates the fraction of metallic SWCNTs in the SWCNT bundle,  $p$  indicates the specularity of the GNR edge. n-GNR and d-GNR represent neutral multilayer GNRs and AsF<sub>5</sub> intercalation-doped multilayer GNRs, respectively.

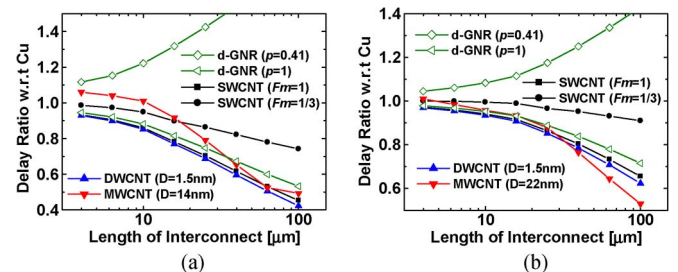


Fig. 18. Signal delay ratios (with respect to Cu) of SWCNT, DWCNT, MWCNT, and different types of GNRs at the intermediate level for the (a) 14-nm and (b) 22-nm technology nodes.  $F_m$  indicates the fraction of metallic SWCNTs in the SWCNT bundle, and  $p$  indicates the specularity of GNR edge. d-GNR represents AsF<sub>5</sub> intercalation-doped multilayer GNRs.

simulation parameters are based on ITRS 2008 [112] prediction and have been summarized in Table III.

Fig. 17 shows the delay ratios of CNT and GNR interconnects with respect to Cu wire at the local level. It can be observed that for most cases, CNT and GNR interconnects have comparable performance to that of Cu, except for monolayer GNR. This is because the driver size at the local level is typically very small ( $= 2$  in this work) and driver resistance dominates the total resistance of the interconnect system. SWCNT, DWCNT and doped GNR ( $p = 1$ ) are slightly better than Cu, while MWCNT is slightly worse than Cu at short lengths but becomes better for lengths  $> 0.5 \mu\text{m}$  due to the smaller capacitance of MWCNT interconnects, as shown in Table III. Monolayer GNRs are much worse than Cu at short lengths due to large quantum contact resistance. Note that the delay of monolayer GNR with  $p = 0.41$  is too large to be shown in the figure. Interestingly, for the case of  $p = 1$ , monolayer GNR starts to outperform Cu after  $2 \mu\text{m}$  because of significantly smaller capacitance than that of Cu as shown in Table III. It should be noted that as the length increases further ( $> 5 \mu\text{m}$ ), the performance of monolayer GNR becomes much worse than that of Cu [91] (due to the range of local interconnect's length, this effect is not shown in Fig. 17).

Fig. 18 shows delay ratios of CNT and GNR interconnects with respect to Cu wire at the intermediate level. It can be observed from Fig. 18 that most CNT interconnects will outperform Cu wire. For ideal case SWCNT and DWCNT, where all SWCNTs and both shells in DWCNT are metallic, they have similar performance, both of them could obtain 30% and 50% delay enhancement at length =  $100 \mu\text{m}$  for 22 and 14 nm, respectively. Even for the metallic fraction  $F_m = 1/3$  case SWCNT, it still can provide better performance than Cu. For the case of MWCNTs, it is slightly worse than Cu at short lengths due to its high resistance when length is  $< 10 \mu\text{m}$ , as shown in Fig. 10, but is significantly better for long lengths due to low resistance as well as slightly smaller capacitance. One interesting finding is that MWCNT could be better than ideal SWCNT or DWCNT for 22 nm but worse than them for 14 nm. This is because the diameter of MWCNT is assumed to be 14 nm at the 14-nm technology node and 22 nm at the 22-nm technology node, and because a larger diameter will have smaller resistivity as shown in [65], MWCNT gives better performance at the 22-nm technology node. For GNR interconnects, the specularity has a very important effect on its performance. For the ideal case, where  $p = 1$ , a doped GNR could provide better performance than that of Cu (but is still worse

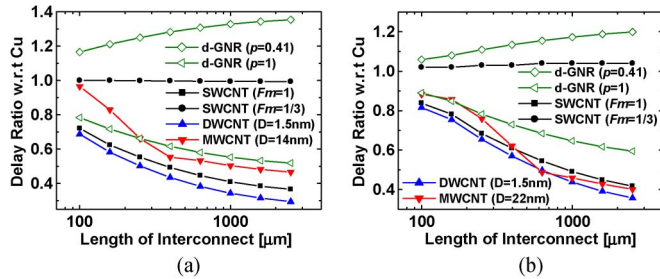


Fig. 19. Signal delay ratios (with respect to Cu) of SWCNT, DWCNT, MWCNT, and different types of GNRs at the global level for the (a) 14-nm and (b) 22-nm technology nodes.  $F_m$  indicates the fraction of metallic SWCNTs in the SWCNT bundle, and  $p$  indicates the specularity of the GNR edge. d-GNR represents AsF<sub>5</sub> intercalation-doped multilayer GNRs.

than the ideal SWCNT and DWCNT), however, if  $p = 0.41$ , which is a more practical case (Cu interconnects have similar specularity value [50]), the delay of doped GNR interconnect could be as much as 40% worse than that of Cu.

Similar results can also be observed for global-level interconnects, as shown in Fig. 19: most CNTs outperform Cu, while a doped GNR with  $p = 0.41$  is worse than Cu. For ideal-case SWCNTs and DWCNTs, where all SWCNTs and shells in the DWCNT are metallic, they have similar performance, both of them could provide more than 50% delay enhancement at length = 1000 μm for the 22- and 14-nm technology nodes. However, at the global level, an SWCNT with  $F_m = 1/3$  is no longer better than Cu; this is because the Cu wire width is large at the global level, and the size effects are less evident. For global interconnects, the ideal-case GNR (doped GNR with  $p = 1$ ) still cannot be better than the ideal-case SWCNT, DWCNT, or MWCNT.

Note that we did not consider monolayer and multilayer neutral GNRs at the intermediate and global levels. This is because at the intermediate and global levels, driver sizes are usually large and the interconnect lengths are long, and as a result, the resistance of the interconnect itself becomes more important than driver resistance. Since monolayer and multilayer neutral GNRs have much higher resistances than other materials, and since their performance is much worse than that of Cu [91], they have been excluded in these figures.

### B. CNT Vias (Vertical Interconnects)

Since for short vertical interconnects (vias), reliability is more critical than performance [52], it is necessary to understand the thermal properties of CNT interconnects and quantify their impact on performance and thermal management of the back-end [128].

For via application, since the height is typically smaller than 300 nm, it can be safely assumed to be both electrically and thermally in the ballistic transport regime [128], since both electron and phonon MFPs of the CNT will be larger than this value (can be seen from Section IV). Therefore, the thermal analysis of CNT vias falls into the ballistic thermal transport regime, where  $\tau_n(q, \omega_n)$  in (27) can be assumed to be 1, and the results shown in Fig. 15 can be utilized. Fig. 20(a) shows a schematic view of a CNT via structure considered in this work, where top (M2) and bottom (M1) metal layers are Cu,

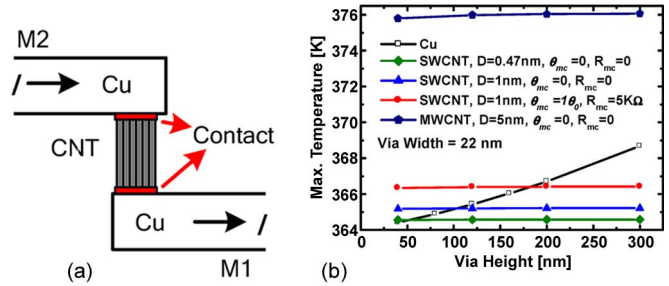


Fig. 20. (a) Schematic view of the simulated square CNT via structure, with top and bottom metal (Cu) layers. The contacts are highlighted as red areas. (b) Maximum temperature rise with increasing via height (with via width = 22 nm) for densely packed CNT vias (for different diameters,  $\theta_{mc}$  and  $R_{mc}$  values) and Cu via.  $\theta_0$  is the ballistic thermal resistance of CNT. Excitation current  $I = 0.142$  mA, and the ambient temperature is assumed to be 363 K.

the vertical via could be CNT, Cu, or tungsten. Rigorous 3-D electrothermal FEM simulations are carried out to examine the thermal profile of this via structure. For CNTs, both thermal contact resistance  $\theta_{mc}$  and electrical contact resistance  $R_{mc}$  between CNT vias and adjacent Cu wires are taken into account along with temperature- and size-dependent Cu resistivity. For ballistic transport, both thermal and electrical resistances remain constant as long as the CNT is shorter than the MFP. This advantage of CNT property can be utilized if it is applied to taller vias (but shorter than the MFP). Fig. 20(b) compares the maximum interconnect temperature rise with CNT vias to that with Cu vias, for increasing via height. An important point to note is that, as the via height is increased, the maximum temperature increases monotonically in case of Cu vias but remains relatively unchanged for CNT vias due to electrically and thermally ballistic transportation. It can be observed that small-diameter SWCNT vias can achieve better thermal performance than Cu vias, even after considering the imperfect thermal contact resistance  $\theta_{mc}$  and the electrical contact resistance  $R_{mc}$  (for via height > 200 nm). However, a Cu via exhibits much better performance than MWCNT vias. It is noteworthy that we also compared CNT with tungsten (W), which is also used as via material today due to its good reliability properties. For the tungsten case with via heights of 40 and 80 nm (resistivity of tungsten is calculated using method in [136]), the maximum temperature of the structure in Fig. 20(a) will be 387.8 and 396.5 K, respectively, which are much larger than those of CNT and Cu cases. Hence, for via application, both MWCNT and SWCNT could be better than tungsten via. However, if objective is to outperform Cu via, small-diameter SWCNT vias with good electrical and thermal contacts is needed.

### C. CNT-Based Inductors

To take advantage of the unique high-frequency properties of CNTs, CNT-based on-chip inductors have been designed and analyzed [31]. For inductor design, quality factor ( $Q$ ) is a very important performance metric. Since CNTs have very large kinetic inductance, one natural question is that, will this large inductance value increase the quality ( $Q$ ) factor of CNT-based inductors accordingly? For CNT-based inductors,  $Q$  factor can be divided into two parts, namely,  $Q_{\text{magnetic}}$  and  $Q_{\text{kinetic}}$ , as shown in Fig. 21(a). The upper bound of  $Q_{\text{kinetic}}$  as a function

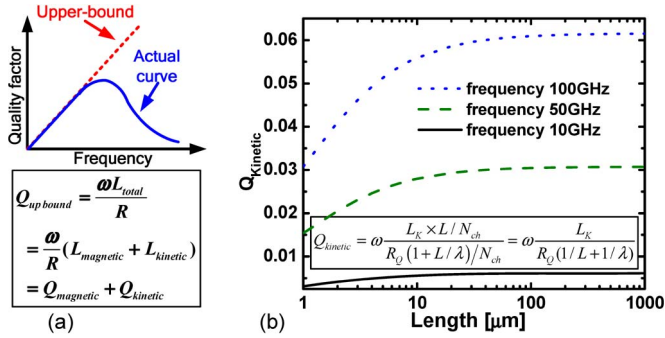


Fig. 21. (a) Schematic view of the  $Q$  factor curve of an inductor. The ideal (upperbound) of  $Q$  factor is  $\omega L/R$ , as shown by the broken line. Due to the presence of parasitic capacitance and conductor/substrate loss, the actual  $Q$  factor curve drops down at high frequencies. (b)  $Q_{kinetic}$  as a function of frequency and length. The equation used for calculating  $Q_{kinetic}$  is shown in the inset.  $\lambda$  is assumed to be  $1 \mu\text{m}$ .

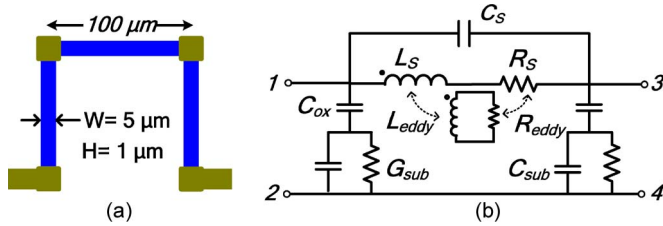


Fig. 22. (a) Structure employed for the ultra-high-frequency inductor, which is 0.75 turn and has an outer diameter of  $100 \mu\text{m}$ , width =  $5 \mu\text{m}$ , and thickness =  $1 \mu\text{m}$ . (b) Equivalent 11 elements  $\pi$  model for on-chip inductors.  $L_S$  and  $R_S$  are the frequency-dependent series inductance and resistance, respectively.  $L_{eddy}$  and  $R_{eddy}$  capture the eddy current effects in the substrate.  $C_S$ ,  $C_{ox}$ , and  $C_{sub}$  are the inter-turn conductor, oxide, and substrate capacitances, respectively.

of length and frequency are calculated and shown in Fig. 21(b). The equation used for the calculation is shown in the inset of Fig. 21(b). It can be observed that although the kinetic inductance of each CNT in a bundle has a very large value, the value of  $Q_{kinetic}$  is negligible ( $< 0.065$  at 100 GHz), as shown in Fig. 21(b). Therefore, in order to achieve high  $Q$  factors (usually  $> 10$ ), the magnetic-field-related inductance still needs to be utilized. Since magnetic inductance depends on the geometry, one cannot shrink the footprint of the inductor. Based on this understanding, Fig. 22(a) shows the schematic view of a three-fourths turn CNT-based on-chip inductor design for a very-high-frequency application (several tens of gigahertz). A metal block at each corner is employed as a contact for CNT bundles along perpendicular directions. A similar structure, in which the CNT bundles are grown along perpendicular directions from a common block, has been fabricated in [28] and is shown in Fig. 8(b).

In the following analysis the  $Q$  factor is defined as

$$Q = -\frac{\text{imag}(Y_{11})}{\text{real}(Y_{11})} \quad (29)$$

where  $Y_{11}$  is the input admittance of the inductor network [across ports 1 and 2 with ports 3 and 4 shorted in Fig. 22(b)].

In order to model the on-chip inductor, the widely used  $\pi$  model [137] is modified to include the effect of the substrate, as shown in Fig. 22(b).  $L_S$  and  $R_S$  are the series frequency-dependent inductance and resistance, respectively,

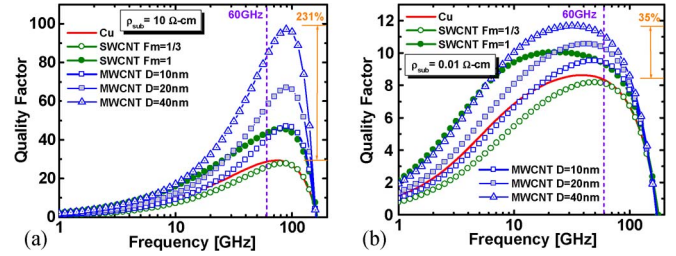


Fig. 23. Quality factor of the inductors [in Fig. 21(a)] based on Cu, SWCNT, and MWCNT interconnects as a function of frequency for (a) low-loss ( $\rho = 10 \Omega \cdot \text{cm}$ ) and (b) high-loss ( $\rho = 0.01 \Omega \cdot \text{cm}$ ) substrate. The thickness of oxide and substrate are assumed to be  $6 \mu\text{m}$  and  $200 \mu\text{m}$ , respectively.  $D$  is the outmost diameter of the MWCNTs.

of CNT interconnects without considering the substrate effect. For CNT-based inductors,  $L_S$  and  $R_S$  can be obtained by employing the impedance extraction procedure discussed in Section IV-D, while for Cu-based inductors, they can be extracted using FastHenry [122]. At high frequencies, the eddy current induced in the substrate will significantly decrease the performance of the inductor. This eddy current, which is in the opposite direction with respect to the current of the inductor, will not only reduce the effective magnetic energy stored in the system, but also increase energy dissipation due to substrate loss. In order to capture the effect of the substrate, complex image theory [138] is employed to calculate  $L_{eddy}$  and  $R_{eddy}$  in Fig. 22(b). The capacitance of inductor is calculated using the distributed model presented in [139].

Based on the model in Fig. 22(b), the performance of the CNT-based inductor structure in Fig. 22(a) can be analyzed and compared to that of Cu inductors [119]. Note that the on-chip inductor has been designed for ultra-high-frequency (tens of gigahertz, e.g., 60 GHz [140]) RF circuit applications. Fig. 23(a) and (b) shows the  $Q$  factor of such inductors at several tens of gigahertz application for different types of CNT bundles and Cu wire. It can be observed that for a low-loss substrate [Fig. 23(a)], the maximum  $Q$  factor of inductor can be increased by as much as 230% (3.3 times) by going from Cu to CNTs. This significant enhancement in  $Q$  factor arises not only because of the lower dc resistance of CNTs, but also because of the reduced skin effect in CNT interconnects, as discussed in Section IV-D (Fig. 14). This is clear from examining the cases of MWCNTs with  $D = 10 \text{ nm}$ , or SWCNT with metallic fraction  $F_m = 1/3$ . Both of these CNT cases have larger resistivity than Cu, however, inductors based on these materials have better or comparable  $Q$  factors than that of a Cu-based inductor. This indicates that a reduced skin effect in CNT bundles can have a significant positive impact on the performance of inductors. For a high-loss substrate [Fig. 23(b)], the substrate starts having negative impact on the inductor, and therefore, the benefit of CNT's high-frequency properties gets eclipsed by large substrate eddy current loss. Nevertheless, CNT inductors still provides better performance than that of Cu except for the case of SWCNT with  $F_m = 1/3$ . The maximum  $Q$  factor enhancement in high-loss substrate is 35% for the case of MWCNT with an outmost diameter of 40 nm. All these results imply that CNTs would be highly promising for high-frequency applications, including on-chip inductor designs.

#### D. CNT-Based Capacitors

As a nanoscale material, one advantage of CNT is its small form factor and high surface-area-to-volume ratio—a very desirable property for capacitor applications [30], [141]. Capacitors are a very important element in many IC circuits, particularly in RF circuits and DRAMs. From ITRS prediction, there is no solution for MIM capacitors to fit future scaling trends, in terms of both capacitance density and leakage [112]. The aspect ratio of present DRAM stacked capacitors is about 30 : 1 and is expected to increase to more than 50 : 1 around 2012. Creating such high-aspect-ratio capacitors with straight walls is an extremely difficult task. Aspect-ratio-dependent etching becomes a serious problem with each new IC generation.

One possible solution for future capacitors is to use a vertical CNT growth process, where the aspect ratio and capacitance density can increase dramatically. As mentioned before, alternative bottom-up process can be implemented for CNT growth [27], which can alleviate the traditional problems associated with etching high aspect-ratio trenches, thereby allowing very-high-aspect-ratio capacitors, which is critical for DRAM application. In addition, due to their small form factor and high surface-area-to-volume ratio, vertical CNT electrodes could also increase the capacitance density (per unit area). However, CNT capacitor also has a negative aspect—a quantum capacitance in series with electrostatic capacitance for each CNT, which reduces the effective total capacitance. Generally, effective total capacitance can be obtained by  $[C_{\text{total}}]^{-1} = [C_E]^{-1} + [C_Q]^{-1}$  [142], where  $[C_E]$  is the electrostatic capacitance matrix, off-diagonal entries in  $[C_Q]$  are zero, and diagonal entries are the quantum capacitance of each CNT ( $C_{\text{QCNT}}$ ), which can be calculated as

$$C_{\text{QCNT}} = \begin{cases} 2C_{Q/\text{channel}}, & \text{SWCNT} \\ \sum_{\text{shells}} M_{\text{shell}}(D_i) \cdot C_{Q/\text{channel}}, & \text{MWCNT} \end{cases} \quad (30)$$

where the  $M_{\text{shell}}$  and  $C_{Q/\text{channel}}$  are given in (8) and (16), respectively and  $D_i$  is the diameter of the  $i$ th shell. In the simple dc cases, if CNTs are assumed to be uniform and have identical quantum capacitance  $C_{\text{QCNT}}$ , total capacitance calculation can be simplified as

$$\frac{1}{C_{\text{total}}} = \frac{1}{C_{E,\text{tot}}} + \frac{1}{N_A C_{\text{QCNT}}} + \frac{1}{N_C C_{\text{QCNT}}} \quad (31)$$

where  $C_{E,\text{tot}}$  is the overall effective electrostatic capacitance, which can be obtained from traditional capacitance extraction tool, such as [118], and  $N_A$  and  $N_C$  are the total number of CNTs of anode and cathode, respectively.

Two feasible vertical-high-aspect-ratio CNT capacitor structures are proposed in Fig. 24. All CNTs are assumed to be MWCNTs with a diameter of 20 nm, and oxide thickness is set to be 20 nm as well. Table IV summarizes the simulated capacitance values of these two configurations of CNT capacitors. For the square structure [Fig. 24(b)], we consider two cases. In one case, CNTs are densely packed along the electrodes (distance between CNTs equal 0.34 nm), while in the other, CNTs are sparsely packed along the electrodes (distance between CNTs equal to 20 nm). Note that in the simulation, the oxide

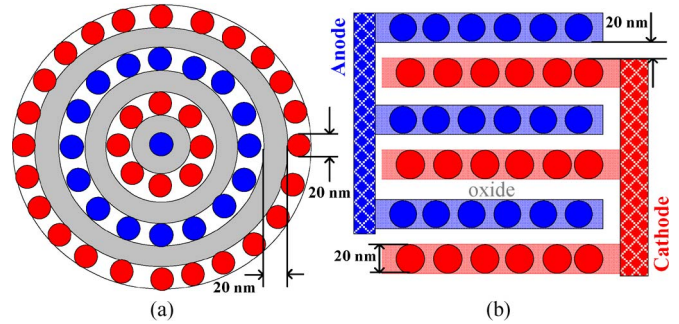


Fig. 24. Two feasible vertical high-aspect-ratio CNT capacitor structures. Red color CNTs are cathode, while blue color CNTs represent anode. The CNTs are assumed to be MWCNT with a diameter of 20 nm. (a) Circular. (b) Square.

TABLE IV  
CNT-BASED CAPACITOR SIMULATION RESULTS

	Electrostatic capacitance density (fF/ $\mu\text{m}^2$ )	Total effective capacitance density (fF/ $\mu\text{m}^2$ )
Circular	31.79	30.65
Square (Dense)	39.48	38.39
Square (Sparse)	30.26	28.99

Oxide material is assumed to be silicon dioxide and height of vertical CNT is assumed to be 1  $\mu\text{m}$ .

material is chosen to be silicon dioxide and the height of the capacitor is assumed to be 1  $\mu\text{m}$ , which can easily be fabricated by a bottom-up approach [27], [30]. If larger dielectric constant oxide is chosen, or a taller vertical CNT is assumed, the capacitance values could even be higher than those shown in Table IV.

From ITRS prediction, MIM capacitors are required to achieve a capacitance density of 7 fF/ $\mu\text{m}^2$  by the year 2014 or 12 fF/ $\mu\text{m}^2$  by 2022 [112]. All the simulated CNT capacitors shown here have much larger capacitance density than the ITRS requirement even after considering the quantum capacitance. It can be observed from Table IV that the square capacitor structure with densely packed CNT electrodes has the highest capacitance density.

#### E. Through-Silicon Vias (TSVs)

A 3-D integration scheme reduces the number and average lengths of the longest global wires seen in traditional planar (2-D) chips, which consequently reduces interconnect delays. In addition, this scheme leads to increased transistor packing density, smaller chip area, and lower power dissipation and provides means to integrate dissimilar technologies (digital, analog, RF circuits, etc) in the same chip [143], [144]. High-aspect-ratio vertical interconnects, called TSVs, providing connectivity between semiconductor layers, constitute a key technology for 3-D ICs. Unlike vias in traditional 2-D technology, TSVs can be 10–100  $\mu\text{m}$  high, with an aspect ratio of 6–20. Depositing Cu or tungsten in such high aspect-ratio but narrow TSVs is very challenging.

On the other hand, it is noteworthy that “bottom-up” growth techniques for CNT vias [27] are inherently better suited for very high aspect-ratio vias than any “top-down” metal deposition technique. Well-aligned high-aspect-ratio CNT bundles have been fabricated in [77], and furthermore, Xu *et al.* [78]

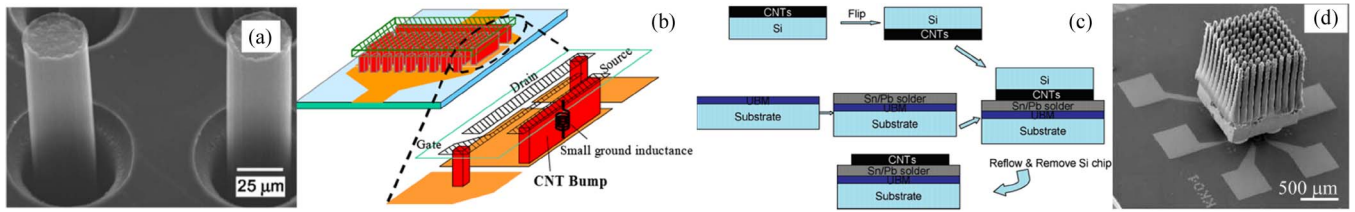


Fig. 25. (a) Two CNT bundles as through-silicon vias [78]. (b) Schematic diagram of flip-chip HPA packaging employing CNT bumps [146]. (c) Process of transferring open-ended CNTs to desired substrates [147]. (d) SEM image of an assembled CNT heat spreader [150].

have developed and demonstrated a process of fabricating CNT-based TSVs [see Fig. 25(a)]. As already discussed in Section IV-E, longer CNTs have higher thermal conductivities, which can be several times larger than those of Cu or W. In addition, since the height of TSVs is typically much larger than the electrical MFP of SWCNTs, or on the same order of the electrical MFP of MWCNTs, the advantage of long MFP of CNT can be utilized. Therefore, the resistance of tall CNT bundle, such as TSVs, could be lower than that of Cu as can be observed in Fig. 10. Moreover, CNT-based TSVs will also have superior high-frequency characteristics with respect to that of Cu [119]. Most recently, an accurate compact ac model has been developed in [145], which is valid for various frequency regimes as well as for different materials including CNTs. Moreover, it is shown specifically that MWCNT based TSVs exhibit better conductance than those of Cu and W based TSVs at high frequencies. Hence, CNT bundles can potentially offer excellent electrical and thermal properties, making them very good candidates for TSVs.

#### F. CNT Chip-to-Packaging Interconnects

In addition to on-chip interconnect application, CNTs can also be used as chip-to-packaging interconnects. The properties of CNTs, such as high current carrying capacity, thermal conductivity, and mechanical strength, are highly favorable for packaging applications. In addition, CNTs can provide fine form factors, which is also preferable for the small size of future input/output pads. Utilizing CNTs as flip-chip bumps for the packaging of high-power amplifiers (HPAs) has been demonstrated in [146]. CNT bumps not only provide low parasitic electrical interconnection for drain, source, and gate, but also provide efficient thermal dissipation path for the heat source (HPA), as shown in Fig. 25(b). Thermal conductivity of CNTs was achieved to be as high as  $1400 \text{ W/m} \cdot \text{K}$ . Because of this high thermal conductivity, the flip-chip structure could be successfully fabricated without degrading thermal performance. In the meantime, because of the absence of long wire bondings, the flip-chip structure has lower parasitic inductance; therefore, it achieves better high-frequency performance, as demonstrated in [146].

A low-temperature approach for CNT soldering for packaging has been proposed in [147]. As shown in Fig. 25(c), this approach first employs high-quality open-ended CNT growth at a high temperature ( $775 \text{ }^\circ\text{C}$ ), followed by CNT adhesion onto the desired substrate at a low temperature ( $270 \text{ }^\circ\text{C}$ ), which is compatible with a microelectronic back-end process. This process could overcome the serious obstacles of integration of

CNTs into ICs and microelectronic packages by offering low process temperatures and improved adhesion of CNTs to the substrates. Several works have also studied the prospects of using CNT as thermal interface materials (TIMs) for packaging [148], [149] and have demonstrated that CNTs can provide lower thermal resistance. Recently, patterned CNTs have been used as a heat spreader for chip cooling [150]. By soldering CNT arrays onto the back side of chips as a heat spreader [see Fig. 25(d)], chip packages can not only achieve better thermal performance compared to Cu cooling structure but also provide a lightweight and mechanically stronger cooling system.

## VI. CONCLUSION

The current status of research on CNT and GNR interconnects, from both fabrication and modeling perspectives, has been reviewed in this paper. From modeling perspective, SWCNT, DWCNT, and MWCNT interconnects can provide better delay performance than that of Cu, particularly for long global wires. However, on the fabrication front, most of the reported progress has been focused on MWCNT-based vertical interconnects (vias). Electrothermal analysis of CNT vias has shown that although CNT vias are both electrically and thermally ballistic, smaller diameter densely packed SWCNTs with good contacts are needed to have better thermal and reliability performance compared to that of the Cu vias. Moreover, taller CNT vias will have better advantages than shorter CNT vias as compared to their metal (Cu or W) counterparts. However, a thermal conductivity model for long-length CNT is still lacking. More experimental and theoretical work is required to fully understand the phonon-scattering mechanisms in non-ballistic CNTs.

While fabricating horizontal long CNT interconnect remains challenging, horizontal GNR interconnects are expected to be easier to fabricate due to their patternability. However, it has been shown that in order for GNR interconnects to be comparable with CNT and Cu interconnects, intercalation-doped multilayer GNRs with high edge-specularity are needed.

High-frequency analysis of CNT interconnects reveals that due to the presence of large kinetic inductance, the skin effect is reduced in a CNT bundle. This unique characteristic of CNT bundle is very important and promising for future high-frequency circuit applications. CNT-based on-chip inductors could offer more than three times quality factor enhancement over Cu-based inductors without using any magnetic material or design optimization. Application of CNT as capacitors is also promising considering their small form factors and easily achievable high-aspect-ratio fabrication process. Our

simulation shows that CNT-based capacitors can achieve more than three times higher capacitance density than that of ITRS requirement in 2022 even with standard SiO<sub>2</sub> dielectric and conservative CNT height of 1 μm. In addition, because of very good electrical and thermal properties, CNTs are also very promising for TSVs in 3-D IC integration as well as for various chip-to-packaging interconnect applications.

#### APPENDIX I WHY ARE ELECTRONS AND HOLES IN GRAPHENE MASSLESS?

The well-known relativistic energy–momentum equation can be expressed as

$$E_{\text{tot}} = \sqrt{P^2 c^2 + m_0^2 c^4} \quad (\text{A1})$$

where  $E_{\text{tot}}$  is the total energy of a particle,  $P$  is the momentum,  $c$  is the speed of light, and  $m_0$  is the rest mass. The kinetic energy  $E_{\text{kin}}$  is the difference between total energy ( $E_{\text{tot}}$ ) of a particle and the rest energy ( $m_0 c^2$ ) of the particle, i.e.,

$$E_{\text{kin}} = E_{\text{tot}} - m_0 c^2 = \sqrt{P^2 c^2 + m_0^2 c^4} - m_0 c^2. \quad (\text{A2})$$

When  $P \ll m_0 c$ , (A2) reduces to

$$E_{\text{kin}} = P^2 / 2m_0 \quad (\text{A3})$$

which implies the nonrelativistic case. In this case,  $E_{\text{kin}}$  is proportional to  $P^2$ . When  $m_0 = 0$  or the particle is massless, (A2) is reduced to

$$E_{\text{kin}} = P c. \quad (\text{A4})$$

In such a case,  $E_{\text{kin}}$  is proportional to  $P$ .

In graphene, since the  $E-k$  relation is linear at low energies, we have

$$|E| = \hbar v_F |\vec{k} - \vec{k}_0| = |\vec{P}| v_F. \quad (\text{A5})$$

Therefore, the electrons and holes in graphene can be considered as massless particles with a “speed of light” of  $v_F$ , which is the Fermi velocity.

It should be noted that for CNTs or GNRs, only the electrons/holes on the subband crossing the Dirac points are massless. The effective mass of electrons/holes on other subbands is nonzero and increases with higher energy subbands.

#### APPENDIX II METALLIC CONDITION OF A CNT

As stated in Section II-B, the band structure of a CNT can be obtained as many slice cuts of (along  $\vec{T}_r$  shown in Fig. 26) the energy dispersion of 2-D graphene. If the slices cut through the Dirac point  $K$ , there is no bandgap in the CNT’s band structure, and the CNT is metallic. Since the distance between each slice cut is  $|\vec{C}_r|$ , the metallic condition requires that the vertical distance between point  $K$  and  $\vec{T}_r(\vec{X}\vec{K})$  be a multiple of  $|\vec{C}_r|$ . As have been proved in [1],  $\vec{X}\vec{K}$  can be written as

$$\vec{X}\vec{K} = \frac{2n + m}{3} \vec{C}_r. \quad (\text{A6})$$

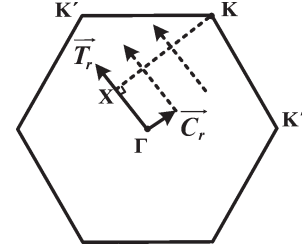


Fig. 26. Brillouin zone of a CNT.  $\vec{T}_r$  is the reciprocal vector of the translation vector  $\vec{T}$ ,  $\vec{C}_r$  is the reciprocal vector of the circumferential vector  $\vec{C}$ , and  $K$  and  $K'$  are the Dirac points.  $\vec{X}\vec{K}$  is the vertical distance from the Dirac point  $K$  to  $\vec{T}_r$ .  $\Gamma$  is the origin of the Brillouin zone of graphene.

Therefore, the condition for a metallic CNT requires that  $(2n + m)$ , or equivalently  $(n - m)$ , be a multiple of 3.

#### ACKNOWLEDGMENT

The authors would like to thank Dr. F. Kreupl, SanDisk Corporation, CA, Dr. A. Cassell, National Aeronautics and Space Administration, Ames, CA, and Dr. M. Nihei, Fujitsu Laboratories, Japan, for many useful discussions and feedback.

#### REFERENCES

- [1] R. Saito, G. Dresselhaus, and S. Dresselhaus, *Physical Properties of Carbon Nanotubes*. London, U. K.: Imperial College Press, 1998.
- [2] S. Iijima, “Helical microtubules of graphitic carbon,” *Nature*, vol. 354, no. 6348, pp. 56–58, Nov. 1991.
- [3] H. W. Kroto, J. R. Heath, S. C. O’Brien, R. F. Curl, and R. E. Smalley, “C60: Buckminsterfullerene,” *Nature*, vol. 318, no. 6042, pp. 162–163, 1985.
- [4] K. S. Novoselov, A. K. Geim, S. V. Morozov, D. Jiang, Y. Zhang, S. V. Dubonos, I. V. Grigorieva, and A. A. Firsov, “Electric field effect in atomically thin carbon films,” *Science*, vol. 306, no. 5696, pp. 666–669, Oct. 2004.
- [5] P. R. Wallace, “The band theory of graphite,” *Phys. Rev.*, vol. 71, no. 9, pp. 622–634, May 1947.
- [6] P. Avouris, Z. Chen, and V. Perebeinos, “Carbon-based electronics,” *Nat. Nanotechnol.*, vol. 2, no. 10, pp. 605–613, Oct. 2007.
- [7] Q. Cao and J. A. Rogers, “Ultrathin films of single-walled carbon nanotubes for electronics and sensors: A review of fundamental and applied aspects,” *Adv. Mater.*, vol. 21, no. 1, pp. 29–53, 2009.
- [8] K. Tsukagoshi, B. W. Alphenaar, and H. Ago, “Coherent transport of electron spin in a ferromagnetically contacted carbon nanotube,” *Nature*, vol. 401, no. 6753, pp. 572–574, Oct. 1999.
- [9] Y.-W. Son, M. L. Cohen, and S. G. Louie, “Half-metallic graphene nanoribbons,” *Nature*, vol. 444, no. 7117, pp. 347–350, Nov. 2006.
- [10] J. A. Misewich, R. Martel, P. Avouris, J. C. Tsang, S. Heinze, and J. Tersoff, “Electrically induced optical emission from a carbon nanotube FET,” *Science*, vol. 300, no. 5620, pp. 783–786, May 2003.
- [11] N. Wang, Z. K. Tang, G. D. Li, and J. S. Chen, “Materials science: Single-walled 4 Å carbon nanotube arrays,” *Nature*, vol. 408, no. 6808, pp. 50–51, Nov. 2000.
- [12] M.-F. Yu, O. Lourie, M. J. Dyer, K. Moloni, T. F. Kelly, and R. S. Ruoff, “Strength and breaking mechanism of multiwalled carbon nanotubes under tensile load,” *Science*, vol. 287, no. 5453, pp. 637–640, Jan. 2000.
- [13] F. Lu, L. Gu, M. J. Meziani, X. Wang, P. G. Luo, L. M. Veca, L. Cao, and Y.-P. Sun, “Advances in bioapplications of carbon nanotubes,” *Adv. Mater.*, vol. 21, no. 2, pp. 139–152, 2009.
- [14] M. I. Katsnelson and K. S. Novoselov, “Graphene: New bridge between condensed matter physics and quantum electrodynamics,” *Solid State Commun.*, vol. 143, no. 1/2, pp. 3–13, Jul. 2007.
- [15] C. Du, J. Yeh, and N. Pan, “High power density supercapacitors using locally aligned carbon nanotube electrodes,” *Nanotechnology*, vol. 16, no. 4, pp. 350–353, Feb. 2005.
- [16] P. Wei, W. Bao, Y. Pu, C. N. Lau, and J. Shi, “Anomalous thermoelectric transport of Dirac particles in graphene,” *Phys. Rev. Lett.*, vol. 102, no. 16, p. 166 808, Apr. 2009.

- [17] H. Ago, K. Petritsch, M. S. P. Shaffer, A. H. Windle, and R. H. Friend, "Composites of carbon nanotubes and conjugated polymers for photovoltaic devices," *Adv. Mater.*, vol. 11, no. 15, pp. 1281–1285, 1999.
- [18] W. B. Choi, D. S. Chung, J. H. Kang, H. Y. Kim, Y. W. Jin, I. T. Han, Y. H. Lee, J. E. Jung, N. S. Lee, G. S. Park, and J. M. Kim, "Fully sealed, high-brightness carbon-nanotube field-emission display," *Appl. Phys. Lett.*, vol. 75, no. 20, pp. 3129–3131, Nov. 1999.
- [19] X. Li, X. Wang, L. Zhang, S. Lee, and H. Dai, "Chemically derived, ultrasmooth graphene nanoribbon semiconductors," *Science*, vol. 319, no. 5867, pp. 1229–1232, Feb. 2008.
- [20] P. G. Collins, M. S. Arnold, and P. Avouris, "Engineering carbon nanotubes and nanotube circuits using electrical breakdown," *Science*, vol. 292, no. 5517, pp. 706–709, Apr. 2001.
- [21] H. W. C. Postma, T. Teepen, Z. Yao, M. Grifoni, and C. Dekker, "Carbon nanotube single-electron transistors at room temperature," *Science*, vol. 293, no. 5527, pp. 76–79, Jul. 2001.
- [22] J. Appenzeller, Y. Lin, J. Knoch, Z. Chen, and P. Avouris, "Comparing carbon nanotube transistors—The ideal choice: A novel tunneling device design," *IEEE Trans. Electron Devices*, vol. 52, no. 12, pp. 2568–2576, Dec. 2005.
- [23] J. E. Jang, S. N. Cha, Y. J. Choi, D. J. Kang, T. P. Butler, D. G. Hasko, J. E. Jung, J. M. Kim, and A. J. Amaratunga, "Nanoscale memory cell based on a nanoelectromechanical switched capacitor," *Nanotechnology*, vol. 3, no. 1, pp. 26–30, Jan. 2008.
- [24] H. Dadgour, A. M. Cassell, and K. Banerjee, "Scaling and variability analysis of CNT-based NEMS devices and circuits with implications for process design," in *IEDM Tech. Dig.*, 2008, pp. 529–532.
- [25] *Hyperion Catalysis*. [Online]. Available: <http://www.fibrils.com>
- [26] F. Kreupl, A. P. Graham, G. S. Duesberg, W. Steinhogel, M. Liebau, E. Unger, and W. Honlein, "Carbon nanotubes in interconnect applications," *Microelectron. Eng.*, vol. 64, no. 1–4, pp. 399–408, Oct. 2002.
- [27] J. Li, Q. Ye, A. Cassell, H. T. Ng, R. Stevens, J. Han, and M. Meyyappan, "Bottom-up approach for carbon nanotube interconnects," *Appl. Phys. Lett.*, vol. 82, no. 15, pp. 2491–2493, Apr. 2003.
- [28] M. Nihei, D. Kondo, A. Kawabata, S. Sato, H. Shioya, M. Sakae, T. Iwai, M. Ohfuti, and Y. Awano, "Low-resistance multi-walled carbon nanotube vias with parallel channel conduction of inner shells," in *Proc. IEEE Int. Interconnect Technol. Conf.*, 2005, pp. 234–236.
- [29] A. Kawabata, S. Sato, T. Nozue, T. Hyakushima, M. Norimatsu, M. Mishima, T. Murakami, D. Kondo, K. Asano, M. Ohfuti, H. Kawarada, T. Sakai, M. Nihei, and Y. Awano, "Robustness of CNT via interconnect fabricated by low temperature process over a high-density current," in *Proc. IEEE Int. Interconnect Technol. Conf.*, 2008, pp. 237–239.
- [30] J. E. Jang, S. N. Cha, Y. Choi, D.-J. Kang, D. G. Hasko, and G. A. J. Amaratunga, "Nanoscale capacitors based on metal–insulator–carbon nanotube–metal (MICNM) structures," in *Proc. ESSDERC*, 2005, pp. 545–547.
- [31] H. Li and K. Banerjee, "High-frequency effects in carbon nanotube interconnects and implications for on-chip inductor design," in *IEDM Tech. Dig.*, 2008, pp. 525–528.
- [32] M. Radosavljević, J. Lefebvre, and A. T. Johnson, "High-field electrical transport and breakdown in bundles of single-wall carbon nanotubes," *Phys. Rev. B, Condens. Matter*, vol. 64, no. 24, p. 241307, Dec. 2001.
- [33] B. Q. Wei, R. Vajtai, and P. M. Ajayan, "Reliability and current carrying capacity of carbon nanotubes," *Appl. Phys. Lett.*, vol. 79, no. 8, pp. 1172–1174, Aug. 2001.
- [34] F. Li, H. M. Cheng, S. Bai, G. Su, and M. S. Dresselhaus, "Tensile strength of single-walled carbon nanotubes directly measured from their macroscopic ropes," *Appl. Phys. Lett.*, vol. 77, no. 20, pp. 3161–3163, Nov. 2000.
- [35] J. Hone, M. Whitney, C. Piskoti, and A. Zettl, "Thermal conductivity of single-walled carbon nanotubes," *Phys. Rev. B, Condens. Matter*, vol. 59, no. 4, p. R2514, 1999.
- [36] C. Yu, L. Shi, Z. Yao, D. Li, and A. Majumdar, "Thermal conductance and thermopower of an individual single-wall carbon nanotube," *Nano Lett.*, vol. 5, no. 9, pp. 1842–1846, Jul. 2005.
- [37] P. Kim, L. Shi, A. Majumdar, and P. L. McEuen, "Thermal transport measurements of individual multiwalled nanotubes," *Phys. Rev. Lett.*, vol. 87, no. 21, p. 215502, Oct. 2001.
- [38] A. A. Balandin, S. Ghosh, W. Bao, I. Calizo, D. Teweldebrhan, F. Miao, and C. N. Lau, "Superior thermal conductivity of single-layer graphene," *Nano Lett.*, vol. 8, no. 3, pp. 902–907, Feb. 2008.
- [39] S. Ghosh, I. Calizo, D. Teweldebrhan, E. P. Pokatilov, D. L. Nika, A. A. Balandin, W. Bao, F. Miao, and C. N. Lau, "Extremely high thermal conductivity of graphene: Prospects for thermal management applications in nanoelectronic circuits," *Appl. Phys. Lett.*, vol. 92, no. 15, p. 151911, Apr. 2008.
- [40] C. L. Kane, E. J. Mele, R. S. Lee, J. E. Fischer, P. Petit, H. Dai, A. Thess, R. E. Smalley, A. R. M. Verschuere, S. J. Tans, and C. Dekker, "Temperature-dependent resistivity of single-wall carbon nanotubes," *Europhys. Lett.*, vol. 41, no. 6, pp. 683–688, Mar. 1998.
- [41] T. Kwano, H. C. Chiamori, M. Suter, Q. Zhou, B. D. Sosnowchik, and L. Lin, "An electrothermal carbon nanotube gas sensor," *Nano Lett.*, vol. 7, no. 12, pp. 3686–3690, Nov. 2007.
- [42] Q. Shao, G. Liu, D. Teweldebrhan, and A. A. Balandin, "High-temperature quenching of electrical resistance in graphene interconnects," *Appl. Phys. Lett.*, vol. 92, no. 20, p. 202108, May 2008.
- [43] J.-Y. Park, S. Rosenblatt, Y. Yaish, V. Sazonova, H. Ustunel, S. Braig, T. A. Arias, P. W. Brouwer, and P. L. McEuen, "Electron–phonon scattering in metallic single-walled carbon nanotubes," *Nano Lett.*, vol. 4, no. 3, pp. 517–520, Feb. 2004.
- [44] H. J. Li, W. G. Lu, J. J. Li, X. D. Bai, and C. Z. Gu, "Multichannel ballistic transport in multiwall carbon nanotubes," *Phys. Rev. Lett.*, vol. 95, no. 8, p. 86601, Aug. 2005.
- [45] K. I. Bolotin, K. J. Sikes, J. Hone, H. L. Stormer, and P. Kim, "Temperature dependent transport in suspended graphene," *Phys. Rev. Lett.*, vol. 101, no. 9, p. 096802, Aug. 2008.
- [46] K. M. Liew, C. H. Wong, X. Q. He, and M. J. Tan, "Thermal stability of single and multi-walled carbon nanotubes," *Phys. Rev. B, Condens. Matter*, vol. 71, no. 7, p. 075424, Feb. 2005.
- [47] C. Lee, X. Wei, J. W. Kysar, and J. Hone, "Measurement of the elastic properties and intrinsic strength of monolayer graphene," *Science*, vol. 321, no. 5887, pp. 385–388, Jul. 2008.
- [48] *Gmelin Handbook of Inorganic and Organometallic Chemistry*, Springer-Verlag, Berlin, Germany, 1968.
- [49] D. Gunlycke, H. M. Lawler, and C. T. White, "Room-temperature ballistic transport in narrow graphene strips," *Phys. Rev. B, Condens. Matter*, vol. 75, no. 8, p. 085418, Feb. 2007.
- [50] W. Steinhogel, G. Schindler, G. Steinlesberger, M. Traving, and M. Engelhardt, "Comprehensive study of the resistivity of copper wires with lateral dimensions of 100 nm and smaller," *J. Appl. Phys.*, vol. 97, no. 2, p. 023706, Dec. 2005.
- [51] S. Im, N. Srivastava, K. Banerjee, and K. E. Goodson, "Scaling analysis of multilevel interconnect temperatures for high performance ICs," *IEEE Trans. Electron Devices*, vol. 52, no. 12, pp. 2710–2719, Dec. 2005.
- [52] N. Srivastava and K. Banerjee, "A comparative scaling analysis of metallic and carbon nanotube interconnections for nanometer scale VLSI technologies," in *Proc. Int. VLSI Multilevel Interconnect Conf.*, 2004, pp. 393–398.
- [53] N. Srivastava and K. Banerjee, "Interconnect challenges for nanoscale electronic circuits," *TMS J. Mater.*, vol. 56, no. 10, pp. 30–31, Oct. 2004.
- [54] K. Banerjee and N. Srivastava, "Are carbon nanotubes the future of VLSI interconnections?" in *Proc. ACM/IEEE Des. Autom. Conf.*, 2006, pp. 809–814.
- [55] C. T. White and J. W. Mintmire, "Fundamental properties of single-wall carbon nanotubes," *J. Phys. Chem. B*, vol. 109, no. 1, pp. 52–65, 2005.
- [56] K. S. Novoselov, A. K. Geim, S. V. Morozov, D. Jiang, M. I. Katsnelson, I. V. Grigorieva, S. V. Dubonos, and A. A. Firsov, "Two-dimensional gas of massless Dirac fermions in graphene," *Nature*, vol. 438, no. 7065, pp. 197–200, Nov. 2005.
- [57] K. Nakada, M. Fujita, G. Dresselhaus, and M. S. Dresselhaus, "Edge state in graphene ribbons: Nanometer size effect and edge shape dependence," *Phys. Rev. B, Condens. Matter*, vol. 54, no. 24, pp. 17954–17961, Dec. 1996.
- [58] L. Malysheva and A. Onipko, *Dispersion of "Dispersionless Band": Comments on L. Brey and H. A. Fertig Paper Electronic States of Graphene Nanoribbons Studied With the Dirac Equation*, May 2008. arXiv:0802.1385v2 [cond-mat.mes-hall].
- [59] Y.-W. Son, M. L. Cohen, and S. G. Louie, "Energy gaps in graphene nanoribbons," *Phys. Rev. Lett.*, vol. 97, no. 21, p. 216803, Nov. 2006.
- [60] T. Yamamoto, S. Watanabe, and K. Watanabe, "Universal features of quantized thermal conductance of carbon nanotubes," *Phys. Rev. Lett.*, vol. 92, no. 7, p. 075502, Feb. 2004.
- [61] H.-Y. Chiu, V. V. Deshpande, H. W. Ch. Postma, N. Lau, C. Miko, L. Forro, and M. Bockrath, "Ballistic phonon thermal transport in multiwalled carbon nanotubes," *Phys. Rev. Lett.*, vol. 95, no. 22, p. 226101, Nov. 2005.
- [62] L. G. C. Rego and G. Kirczenow, "Quantized thermal conductance of dielectric quantum wires," *Phys. Rev. Lett.*, vol. 81, no. 1, pp. 232–235, 1998.

- [63] C. Kittel, *Introduction to Solid State Physics*, 8th ed. New York: Wiley, 2004.
- [64] N. Srivastava and K. Banerjee, "Performance analysis of carbon nanotube interconnects for VLSI applications," in *Proc. IEEE/ACM Int. Conf. ICCAD*, 2005, pp. 383–390.
- [65] H. Li, W. Y. Yin, K. Banerjee, and J. F. Mao, "Circuit modeling and performance analysis of multi-walled carbon nanotube interconnects," *IEEE Trans. Electron Devices*, vol. 55, no. 6, pp. 1328–1337, Jun. 2008.
- [66] A.-C. Dupuis, "The catalyst in the CCVD of carbon nanotubes—A review," *Prog. Mater. Sci.*, vol. 50, no. 8, pp. 929–961, Nov. 2005.
- [67] A. P. Graham, G. S. Duesberg, W. Hoenlein, F. Kreupl, M. Liebau, R. Martin, B. Rajasekharan, W. Pamler, R. Seidel, W. Steinhögl, E. Unger, "How do carbon nanotubes fit into the semiconductor roadmap?" *Appl. Phys. A, Solids Surf.*, vol. 80, no. 6, pp. 1141–1151, Mar. 2005.
- [68] D. N. Futaba, K. Hata, T. Namai, T. Yamada, K. Mizuno, Y. Hayamizu, M. Yumura, and S. Iijima, "84% catalyst activity of water-assisted growth of single walled carbon nanotube forest characterization by a statistical and macroscopic approach," *J. Phys. Chem. B*, vol. 110, no. 15, pp. 8035–8038, Mar. 2006.
- [69] Y. Maeda, S. Kimura, M. Kanda, Y. Hirashima, T. Hasegawa, T. Wakahara, Y. Lian, T. Nakahodo, T. Tsuchiya, T. Akasaka, J. Lu, X. Zhang, Z. Gao, Y. Yu, S. Nagase, S. Kazaoui, N. Minami, T. Shimizu, H. Tokumoto, and R. Saito, "Large-scale separation of metallic and semiconducting single-walled carbon nanotubes," *J. Amer. Chem. Soc.*, vol. 127, no. 29, pp. 10287–10290, Jul. 2005.
- [70] D. N. Futaba, K. Hata, T. Yamada, T. Hiraoka, Y. Hayamizu, Y. Kakudate, O. Tanaike, H. Hatori, M. Yumura, and S. Iijima, "Shape-engineerable and highly densely packed single-walled carbon nanotubes and their application as super-capacitor electrodes," *Nat. Mater.*, vol. 5, pp. 987–994, 2006.
- [71] Y. Hayamizu, T. Yamada, K. Mizuno, R. C. Davis, D. N. Futaba, M. Yumura, and K. Hata, "Integrated three-dimensional microelectro-mechanical devices from processable carbon nanotube wafers," *Nat. Nanotechnol.*, vol. 3, no. 5, pp. 289–294, May 2008.
- [72] Y. M. Choi, S. Lee, H. S. Yoon, M. S. Lee, H. Kim, I. Han, Y. Son, I. S. Yeo, U.-I. Chung, and J. T. Moon, "Integration and electrical properties of carbon nanotube array for interconnect applications," in *Proc. IEEE Conf. Nanotechnol.*, 2006, pp. 262–265.
- [73] M. Nihei, M. Horibe, A. Kawabata, and Y. Awano, "Simultaneous formation of multiwall carbon nanotubes and their end-bonded ohmic contacts to Ti electrodes for future ULSI interconnects," *Jpn. J. Appl. Phys.*, vol. 43, no. 4B, pp. 1856–1859, 2004.
- [74] F. Kreupl, A. P. Graham, M. Liebau, G. S. Duesberg, R. Seidel, and E. Unger, "Carbon nanotubes for interconnect applications," in *IEDM Tech. Dig.*, 2004, pp. 683–686.
- [75] S. Sato, M. Nihei, A. Mimura, A. Kawabata, D. Kondo, H. Shioya, T. Iwai, M. Mishima, M. Ohfuti, and Y. Awano, "Novel approach to fabricating carbon nanotube via interconnects using size-controlled catalyst nanoparticles," in *Proc. Interconnect Technol. Conf.*, 2006, pp. 230–232.
- [76] M. Nihei, T. Hyakushima, S. Sato, T. Nozue, M. Norimatsu, M. Mishima, T. Murakami, D. Kondo, A. Kawabata, M. Ohfuti, and Y. Awano, "Electrical properties of carbon nanotube via interconnects fabricated by novel damascene process," in *Proc. Interconnect Technol. Conf.*, 2007, pp. 204–206.
- [77] L. Zhu, J. Xu, Y. Xiu, Y. Sun, D. W. Hess, and C. P. Wong, "Growth and electrical characterization of high-aspect-ratio carbon nanotube arrays," *Carbon*, vol. 44, no. 2, pp. 253–258, Feb. 2006.
- [78] T. Xu, Z. Wang, J. Miao, X. Chen, and C. M. Tan, "Aligned carbon nanotubes for through-wafer interconnects," *Appl. Phys. Lett.*, vol. 91, no. 4, p. 042 108, Jul. 2007.
- [79] Z. Liu, N. Bajwa, L. Ci, S. H. Lee, S. Kar, P. M. Ajayan, and J.-Q. Lu, "Densification of carbon nanotube bundles for interconnect application," in *Proc. IEEE Int. Interconnect Technol. Conf.*, 2007, pp. 201–203.
- [80] B. Q. Wei, R. Vajtai, Y. Jung, J. Ward, Y. Zhang, G. Ramanath, and P. M. Ajayan, "Organized assembly of carbon nanotubes," *Nature*, vol. 416, no. 6880, pp. 495–496, Apr. 2002.
- [81] S. Huang, X. Cai, and J. Liu, "Growth of millimeter-long and horizontally aligned single-walled carbon nanotubes on flat substrates," *J. Amer. Chem. Soc.*, vol. 125, no. 19, pp. 5636–5637, Apr. 2003.
- [82] H. Xin and A. T. Woolley, "Directional orientation of carbon nanotubes on surfaces using a gas flow cell," *Nano Lett.*, vol. 4, no. 8, pp. 1481–1484, Aug. 2004.
- [83] A. Nojeh, A. Ural, R. F. Pease, and H. Dai, "Electric-field-directed growth of carbon nanotubes in two dimensions," *J. Vac. Sci. Technol. B, Microelectron. Process. Phenom.*, vol. 22, no. 6, pp. 3421–3425, Dec. 2004.
- [84] Y. H. Yan, S. Li, L. Q. Chen, M. B. Chan-Park, and Q. Zhang, "Large-scale submicron horizontally aligned single-walled carbon nanotube surface arrays on various substrates produced by a fluidic assembly method," *Nanotechnology*, vol. 17, no. 22, pp. 5696–5701, Nov. 2006.
- [85] G. Aichmayr, A. Avellán, G. S. Duesberg, F. Kreupl, S. Kudelka, M. Liebau, A. Orth, A. Sängler, J. Schumann, and O. Störbeck, "Carbon/high-k trench capacitor for the 40 nm DRAM generation," in *Proc. IEEE Symp. VLSI Technol.*, Jun. 2007, pp. 186–187.
- [86] C. Berger, Z. Song, X. Li, X. Wu, N. Brown, C. Naud, D. Mayou, T. Li, J. Hass, A. N. Marchenkov, E. H. Conrad, P. N. First, and W. A. de Heer, "Electronic confinement and coherence in patterned epitaxial graphene," *Science*, vol. 312, no. 5777, pp. 1191–1196, Apr. 2006.
- [87] J. Hass, R. Feng, T. Li, X. Li, Z. Zong, W. A. de Heer, P. N. First, E. H. Conrad, C. A. Jeffrey, and C. Berger, "Highly ordered graphene for two dimensional electronics," *Appl. Phys. Lett.*, vol. 89, no. 14, p. 143 106, Oct. 2006.
- [88] J. C. Meyer, A. K. Geim, M. I. Katsnelson, K. S. Novoselov, T. J. Booth, and S. Roth, "The structure of suspended graphene sheets," *Nature*, vol. 446, no. 7131, pp. 60–63, Mar. 2007.
- [89] Q. Yu, J. Lian, S. Siriponglert, H. Li, Y. P. Chen, and S.-S. Pei, "Graphene segregated on Ni surfaces and transferred to insulators," *Appl. Phys. Lett.*, vol. 93, no. 11, p. 113 103, Nov. 2008.
- [90] X. Li, W. Cai, J. An, S. Kim, J. Nah, D. Yang, R. Piner, A. Velamakanni, I. Jung, E. Tutuc, S. K. Banerjee, L. Colombo, and R. S. Ruoff, "Large-area synthesis of high-quality and uniform graphene films on copper foils," *Science*, vol. 324, no. 5932, p. 1312, May 2009.
- [91] C. Xu, H. Li, and K. Banerjee, "Graphene nano-ribbon (GNR) interconnects: A genuine contender or a delusive dream?" in *IEDM Tech. Dig.*, 2008, pp. 201–204.
- [92] J. E. Fischer and T. E. Thompson, "Graphite intercalation compounds," *Phys. Today*, vol. 31, no. 7, pp. 36–45, Jul. 1978.
- [93] M. S. Dresselhaus and G. Dresselhaus, "Intercalation compounds of graphite," *Adv. Phys.*, vol. 51, no. 1, pp. 1–186, Jan. 2002.
- [94] J. Shioya, H. Matsubara, and S. Murakami, "Properties of AsF<sub>5</sub>-intercalated vapor-grown graphite," *Synth. Met.*, vol. 14, no. 1/2, pp. 113–123, Mar. 1986.
- [95] D. Kondo, S. Sato, and Y. Awano, "Self-organization of novel carbon composite structure: Graphene multi-layers combined perpendicularly with aligned carbon nanotubes," *Appl. Phys. Express*, vol. 1, no. 7, p. 074 003, 2008.
- [96] A. Nieuwoudt and Y. Massoud, "On the impact of process variations for carbon nanotube bundles for VLSI interconnect," *IEEE Trans. Electron Devices*, vol. 54, no. 3, pp. 445–446, Mar. 2007.
- [97] S. Datta, *Electronic Transport in Mesoscopic Systems*. Cambridge, U.K.: Cambridge Univ. Press, 1995.
- [98] H. Stahl, J. Appenzeller, R. Martel, P. Avouris, and B. Lengeler, "Inter-tube coupling in ropes of single-wall carbon nanotubes," *Phys. Rev. Lett.*, vol. 85, no. 24, pp. 5186–5189, Dec. 2000.
- [99] C. T. White and T. N. Todorov, "Carbon nanotubes as long ballistic conductors," *Nature*, vol. 393, pp. 240–242, 1998.
- [100] J. Jiang, J. Dong, H. T. Yang, and D. Y. Xing, "Universal expression for localization length in metallic carbon nanotubes," *Phys. Rev. B, Condens. Matter*, vol. 64, no. 4, p. 045 409, Jul. 2001.
- [101] S. Roche, J. Jiang, L. F. Torres, and R. Saito, "Charge transport in carbon nanotubes: Quantum effects of electron-phonon coupling," *J. Phys., Condens. Matter*, vol. 19, no. 18, p. 183 203, Apr. 2007.
- [102] N. Srivastava, H. Li, F. Kreupl, and K. Banerjee, "On the applicability of single-walled carbon nanotubes as VLSI interconnects," *IEEE Trans. Nanotechnol.*, vol. 8, no. 4, pp. 542–559, Jul. 2009.
- [103] A. Naeemi and J. D. Meindl, "Compact physical models for multiwall carbon-nanotube interconnects," *IEEE Electron Device Lett.*, vol. 27, no. 5, pp. 338–340, May 2006.
- [104] M. Kociak, K. Suenaga, K. Hirahara, Y. Saito, T. Nakahira, and S. Iijima, "Linking chiral indices and transport properties of double-walled carbon nanotubes," *Phys. Rev. Lett.*, vol. 89, no. 15, p. 155 501, Oct. 2002.
- [105] V. Zolyomi, J. Koltai, A. Rusznyak, J. Kurti, A. Gali, F. Simon, H. Kuzmany, A. Szabados, and P. R. Surjan, "Intershell interaction in double walled carbon nanotubes: Charge transfer and orbital mixing," *Phys. Rev. B, Condens. Matter*, vol. 77, no. 24, p. 245 403, Jun. 2008.
- [106] A. Naeemi and J. D. Meindl, "Performance benchmarking for graphene nanoribbon, carbon nanotube, and Cu interconnects," in *Proc. IEEE Int. Interconnect Technol. Conf.*, San Francisco, CA, 2008, pp. 183–185.
- [107] C. Xu, H. Li, and K. Banerjee, "Modeling, analysis and design of graphene nano-ribbon interconnects," *IEEE Trans. Electron Devices*, vol. 56, no. 8, pp. 1567–1578, Aug. 2009.

- [108] D. A. Areshkin, D. Gunlycke, and C. T. White, "Ballistic transport in graphene nanostrips in the presence of disorder: Importance of edge effects," *Nano Lett.*, vol. 7, no. 1, pp. 204–210, Jan. 2007.
- [109] L. Ci, Z. Xu, L. Wang, W. Gao, F. Ding, K. Kelly, B. Yakobson, and P. Ajayan, "Controlled nanocutting of graphene," *Nano Res.*, vol. 1, no. 2, pp. 116–122, Aug. 2008.
- [110] L. X. Benedict, V. H. Crespi, S. G. Louie, and M. L. Cohen, "Static conductivity and superconductivity of carbon nanotubes: Relations between tubes and sheets," *Phys. Rev. B, Condens. Matter*, vol. 52, no. 20, pp. 14 935–14 940, Nov. 1995.
- [111] J. Hass, F. Varchon, J. E. Millán-Otoya, M. Sprinkle, N. Sharma, W. A. de Heer, C. Berger, P. N. First, L. Magaud, and E. H. Conrad, "Why multilayer graphene on 4H-SiC (0001) behaves like a single sheet of graphene," *Phys. Rev. Lett.*, vol. 100, no. 12, p. 125 504, Mar. 2008.
- [112] *International Technology Roadmap for Semiconductors*, 2008. [Online]. Available: <http://public.itrs.net/>
- [113] P. J. Burke, "Luttinger liquid theory as a model of the gigahertz electrical properties of carbon nanotubes," *IEEE Trans. Nanotechnol.*, vol. 1, no. 3, pp. 129–144, Sep. 2002.
- [114] M. W. Bockrath, "Carbon nanotube electrons in one dimension," Ph.D. dissertation, Univ. California, Berkeley, CA, 1999.
- [115] M. P. Anantram and F. Léonard, "Physics of carbon nanotube electronic devices," *Rep. Prog. Phys.*, vol. 69, no. 3, pp. 507–561, Feb. 2006.
- [116] S. Salahuddin, M. Lundstrom, and S. Datta, "Transport effects on signal propagation in quantum wires," *IEEE Trans. Electron Devices*, vol. 52, no. 8, pp. 1734–1742, Aug. 2005.
- [117] A. Naeemi and J. D. Meindl, "Design and performance modeling for single-walled carbon nanotubes as local, semiglobal, and global interconnects in gigascale integrated systems," *IEEE Trans. Electron Devices*, vol. 54, no. 1, pp. 26–37, Jan. 2007.
- [118] S. V. Maxwell, Ansoft Corp. [Online]. Available: <http://www.ansoft.com/maxwells/>
- [119] H. Li and K. Banerjee, "High-frequency analysis of carbon nanotube interconnects and implications for on-chip inductor design," *IEEE Trans. Electron Devices*, 2009, to be published.
- [120] J. J. Plombon, K. P. O'Brien, F. Gstrein, and M. Dubin, "High-frequency electrical properties of individual and bundled carbon nanotubes," *Appl. Phys. Lett.*, vol. 90, no. 6, p. 063 106, Feb. 2007.
- [121] F. W. Grover, *Inductance Calculations*. New York: Dover, 2004.
- [122] M. Kamon, M. J. Tsuk, and J. White, "FastHenry: A multipole-accelerated 3-D inductance extraction program," *IEEE Trans. Microw. Theory Tech.*, vol. 42, no. 9, pp. 1750–1758, Sep. 1994.
- [123] N. W. Ashcroft and N. D. Mermin, *Solid State Physics*. Philadelphia, PA: Saunders College, 1976.
- [124] E. H. Sondheimer, "The mean free path of electrons in metals," *Adv. Phys.*, vol. 50, no. 6, pp. 499–537, Sep. 2001.
- [125] N. Srivastava, R. V. Joshi, and K. Banerjee, "Carbon nanotube interconnect: Implications for performance, power dissipation and thermal management," in *IEDM Tech. Dig.*, 2005, pp. 257–260.
- [126] J. Wang and J.-S. Wang, "Carbon nanotube thermal transport: Ballistic to diffusive," *Appl. Phys. Lett.*, vol. 88, no. 11, p. 111 909, Mar. 2006.
- [127] R. Saito, T. Takeya, and T. Kimura, "Raman intensity of single-wall carbon nanotubes," *Phys. Rev. B, Condens. Matter*, vol. 57, no. 7, pp. 4145–4153, Feb. 1998.
- [128] H. Li, N. Srivastava, W. Y. Yin, J. F. Mao, and K. Banerjee, "Carbon nanotube vias: A reality check," in *IEDM Tech. Dig.*, 2007, pp. 207–210.
- [129] S. Maruyama, "A molecular dynamics simulation of heat conduction of a finite length single-walled carbon nanotube," *Microscale Thermophys. Eng.*, vol. 7, no. 1, pp. 41–50, 2003.
- [130] N. Mingo and D. A. Broido, "Carbon nanotube ballistic thermal conductance and its limits," *Phys. Rev. Lett.*, vol. 95, no. 9, p. 096 105, Aug. 2005.
- [131] N. Mingo and D.A. Broido, "Length dependence of carbon nanotube thermal conductivity and the 'problem of long waves'," *Nano Lett.*, vol. 5, no. 7, pp. 1221–1225, Jul. 2005.
- [132] E. Pop, D. Mann, Q. Wang, K. Goodson, and H. Dai, "Thermal conductance of an individual single-wall carbon nanotube above room temperature," *Nano Lett.*, vol. 6, no. 1, pp. 96–100, Jan. 2006.
- [133] G. Miano and F. Villone, "An integral formulation for the electro-dynamics of metallic carbon nanotubes based on a fluid model," *IEEE Trans. Antennas Propag.*, vol. 54, no. 10, pp. 2713–2724, Oct. 2006.
- [134] J. J. Weststrom, "Signal propagation in electron waveguides: Transmission-line analogies," *Phys. Rev. B, Condens. Matter*, vol. 54, no. 16, pp. 11 484–11 491, Oct. 1996.
- [135] M. S. Sarto, A. Tamburrano, and M. D'Amore, "New electron-waveguide-based modeling for carbon nanotube interconnects," *IEEE Trans. Nanotechnol.*, vol. 8, no. 2, pp. 214–225, Mar. 2009.
- [136] M. Traving, G. Schindler, and M. Engelhardt, "Damascene and subtractive processing of narrow tungsten lines: Resistivity and size effect," *J. Appl. Phys.*, vol. 100, no. 9, p. 094 325, Nov. 2006.
- [137] P. C. Yue and S. Wong, "Physical modeling of spiral inductors on silicon," *IEEE Trans. Electron Devices*, vol. 47, no. 3, pp. 560–568, Mar. 2001.
- [138] A. Weisshaar and A. Luoh, "Closed-form expressions for the series impedance parameters of on-chip interconnects on multilayer silicon substrates," *IEEE Trans. Adv. Packag.*, vol. 27, no. 1, pp. 126–134, Feb. 2004.
- [139] C. Wu, C. Tang, and S. Liu, "Analysis of on-chip spiral inductors using the distributed capacitance model," *IEEE J. Solid-State Circuits*, vol. 38, no. 6, pp. 1040–1044, Jun. 2003.
- [140] B. Razavi, "A 60-GHz CMOS receiver front-end," *IEEE J. Solid-State Circuits*, vol. 41, no. 1, pp. 17–22, Jan. 2006.
- [141] M. Budnik, A. Raychowdury, A. Bansal, and K. Roy, "A high density, carbon nanotube capacitor for decoupling applications," in *Proc. ACM/IEEE Des. Autom. Conf.*, 2006, pp. 935–938.
- [142] C. Kshirsagar, H. Li, T. Kopley, and K. Banerjee, "Accurate intrinsic gate capacitance model for carbon nanotube-array based FETs considering screening effect," *IEEE Electron Device Lett.*, vol. 29, no. 12, pp. 1408–1411, Dec. 2008.
- [143] K. Banerjee, S. J. Souri, P. Kapur, and K. C. Saraswat, "3-D ICs: A novel chip design for improving deep submicron interconnect performance and systems-on-chip integration," *Proc. IEEE*, vol. 89, no. 5, pp. 602–633, May 2001.
- [144] G. L. Loi, B. Agrawal, N. Srivastava, S.-C. Lin, T. Sherwood, and K. Banerjee, "A thermally-aware performance analysis of vertically integrated (3-D) processor-memory hierarchy," in *Proc. 43th ACM/IEEE DAC*, 2006, pp. 991–996.
- [145] C. Xu, H. Li, R. Suaya, and K. Banerjee, "Compact AC modeling and analysis of Cu, W, and CNT based through-silicon vias (TSVs) in 3-D ICs," in *IEDM Tech. Dig.*, 2009, to be published.
- [146] T. Iwai, H. Shioya, D. Kondo, S. Hirose, A. Kawabata, S. Sato, M. Nihei, T. Kikkawa, K. Joshin, Y. Awano, and N. Yokoyama, "Thermal and source bumps utilizing carbon nanotubes for flip-chip high power amplifiers," in *IEDM Tech. Dig.*, 2005, pp. 257–260.
- [147] L. Zhu, Y. Sun, D. W. Hess, and C. P. Wong, "Well-aligned open-ended carbon nanotube architectures: An approach for device assembly," *Nano Lett.*, vol. 6, no. 2, pp. 243–247, Feb. 2006.
- [148] K. Zhang and M. M. F. Yuen, "Heat spreader with aligned CNTs designed for thermal management of HB-LED packaging and microelectronic packaging," in *Proc. 7th Int. Conf. Electron. Packag. Technol.*, 2006, pp. 1–4.
- [149] T. Tong, Y. Zhao, L. Delzeit, A. Kashani, M. Meyyappan, and A. Majumdar, "Dense vertically aligned multiwalled carbon nanotube arrays as thermal interface materials," *IEEE Trans. Compon. Packag. Technol.*, vol. 30, no. 1, pp. 92–100, Mar. 2007.
- [150] K. Kordas, G. Toth, P. Moilanen, M. Kumpumaki, J. Vahakangas, A. Unsimaki, R. Vajtai, and P. M. Ajayan, "Chip cooling with integrated carbon nanotube microfin architectures," *Appl. Phys. Lett.*, vol. 90, no. 12, p. 123 105, Mar. 2007.



**Hong Li** (S'07) received the B.E. degree in electronic engineering from Nanjing University of Aeronautics and Astronautics, Nanjing, China, in 2003 and the M.S. degree from Shanghai Jiao Tong University, Shanghai, China, in 2008. He has been working toward the Ph.D. degree in Professor Banerjee's Nanoelectronics Research Laboratory in the Department of Electrical and Computer Engineering, University of California, Santa Barbara (UCSB), since 2007.

His research interests include the modeling and design of carbon nanomaterials for electronic applications, particularly VLSI interconnects and passive devices. Since December 2008, he has been the Lead Graduate Student working on the development of a state-of-the-art carbon nanomaterial fabrication facility at UCSB's California NanoSystems Institute (CNSI).

Mr. Li received numerous awards for outstanding academic performance, including the Excellent Bachelor's Thesis Award, during his undergraduate years.



**Chuan Xu** (S'08) received the B.S. degree in microelectronics and the M.S. degree in microelectronics and solid-state electronics from Peking University, Beijing, China, in 2004 and 2007, respectively. He is currently working toward the Ph.D. degree in Prof. Banerjee's Nanoelectronics Research Laboratory, Department of Electrical and Computer Engineering, University of California, Santa Barbara. During his M.S. degree, he worked on the fabrication and characterization of AlGaIn/GaN heterostructure field-effect transistors.

During the summer of 2008, he was an Intern with the Electrical Interconnect and Packaging Group, IBM T. J. Watson Research Center, Yorktown Heights, NY. His current research is focused on the modeling, design, and characterization of emerging interconnect materials, structures, and effects.

Mr. Xu was the recipient of the "2008 IBM Problem Solving Award Based on the Use of the EIP Tool Suite," which recognizes outstanding contributions by students in solving the most interesting problems using IBM's Electromagnetic Field Solver Suite of Tools called the EIP tools.



**Navin Srivastava** (S'03) received the B.Tech. (Hons.) degree in electrical engineering from the Indian Institute of Technology, Kharagpur, India, in 2000, and the M.S. and Ph.D. degrees in electrical and computer engineering from the University of California, Santa Barbara, in 2006 and 2009, respectively.

From 2000 to 2003, he was with Atrenta Inc., India. He is currently with the Calibre Division, Mentor Graphics Corporation, Wilsonville, OR. His research interests include VLSI interconnects in

nanoelectronic circuits.

Dr. Srivastava received the Outstanding Graduate Student Paper Award at the VLSI Multilevel Interconnect Conference in 2005 and the IEEE Micro Top Picks Award in 2006.



**Kaustav Banerjee** (S'92–M'99–SM'03) received the Ph.D. degree in electrical engineering and computer sciences from the University of California, Berkeley, in 1999.

In July 2002, he joined the Faculty of the Department of Electrical and Computer Engineering, University of California, Santa Barbara, where he has been a Full Professor since 2007. He is also an affiliated faculty at the California NanoSystems Institute (CNSI) at UCSB. From 1999 to 2001, he was a Research Associate with the Center for Integrated Systems, Stanford University, Stanford, CA. From February to August 2002, he was a Visiting Faculty with the Circuit Research Laboratories, Intel, Hillsboro, OR. He has also held summer/visiting positions at Texas Instruments Incorporated, Dallas, from 1993 to 1997, and the Swiss Federal Institute of Technology, Lausanne, Switzerland, in 2001. He is the author of over 170 journal and refereed international conference papers and two book chapters on 3-D ICs. He is also a coeditor of the book *Emerging Nanoelectronics: Life With and After CMOS* (Springer, 2004). His current research interests include nanometer-scale issues in VLSI as well as circuits and systems issues in emerging nanoelectronics. He is also involved in exploring the design and fabrication of various nanomaterials for ultra energy-efficient electronics and energy harvesting/storage applications.

Prof. Banerjee received numerous awards in recognition of his work, including a Best Paper Award at the Design Automation Conference in 2001, the Association of Computing Machinery (ACM) Special Interest Group on Design Automation Outstanding New Faculty Award in 2004, an IEEE Micro Top Picks Award in 2006, and an IBM Faculty Award in 2008. He has served on the Technical Program Committees of several leading IEEE and ACM conferences, including International Electron Devices Meeting, Design Automation Conference, International Conference on Computer Aided Design, and International Reliability Physics Symposium. From 2005 to 2008, he served as a member of the Nanotechnology Committee of the IEEE Electron Devices Society. He has also served on the Organizing Committee of IEEE International Symposium on Quality Electronic Design at various positions, including Technical Program Chair in 2002 and General Chair in 2005. He is a Distinguished Lecturer of the IEEE Electron Devices Society.